CIMSS

COOPERATIVE INSTITUTE FOR METEOROLOGICAL SATELLITE STUDIES
Space Science and Engineering Center
University of Wisconsin—Madison
1225 West Dayton Street
Madison, Wisconsin 53706
Telex: 265 452 UOFWISC MDS

June 14, 1997

Dr. Gary Toller
SAIC/GSC
6100 Chevy Chase Dr.
Suite 200
Laurel, Md. 20707-2929
Tel. 301 953-2700
FAX 301 953-1213
toller@mrslate.gsc.saic.com
adeos2@cpqm.saic.com

Dear Dr. Toller;

Enclosed is our 1st year interim report for our cloud masking project for GLI. The first draft of the ATBD is also enclosed. The ATBD will be up-dated following the up-coming meeting in September. The version 1 code has been delivered to EORC and as passed preliminary testing.

Sincerely
Steven A. Ackerman

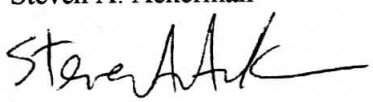

Final interim report for the Pre-launch Standard Product Cloud Mask Algorithm Development for GLI aboard ADEOS II. This report covers first year research activities of the GLI cloud masking algorithm (ATSK1, ATSK2) development.

Description of Activities

Dr. Ackerman attended the 2nd GLI Workshop was held at the Kinugawa Onsen Hotel from June 11 through June 14, 1997 where the cloud masking algorithm was discussed with GLI scientists. As a follow-up of GLI Workshop, the 16 bit, 1km cloud mask was defined as a new Standard Product. The 16 bit structure is currently:

16 BIT GLI CLOUD MASK FILE SPECIFICATION		
BIT FIELD	**DESCRIPTION KEY**	**RESULT**
0-1	Unobstructed FOV Quality Flag	00 = cloudy 01 = probably clear 10 = confident clear 11 = high confidence clear
PROCESSING PATH FLAGS		
2	Day / Night Flag	0 = Night / 1 = Day
3	Sun glint Flag	0 = Yes / 1 = No
4	Snow / Ice Background Flag	0 = Yes/ 1 = No
5-6	Land / Water Flag	00 = Water 01 = Coastal 10 = Desert 11 = Land
ADDITIONAL FLAGS		
7	Non-cloud obstruction Flag (heavy aerosol)	0 = Yes / 1 = No
8	Thin Cirrus Detected (solar)	0 = Yes / 1 = No
9	Shadow Detected	0 = Yes / 1 = No
1-km CLOUD FLAGS		
10	Result from Group I tests	0 = Yes / 1 = No
12	Result from Group II tests	0 = Yes / 1 = No
13	Result from Group III tests	0 = Yes / 1 = No
14	Result from Group IV tests	0 = Yes / 1 = No
15	Result from Group V tests	0 = Yes / 1 = No

Issues and Problems

Since the workshop, we have discussed the issue of using the 250m 1.64 μm channel in cloud masking with Dr. Takashi Nakajima. We conducted experiments with and without this channel in our cloud masking algorithm, and have removed it from the tests. The channel is particularly useful for separating clouds from clear when the surface is snow covered. Tradeoffs of data storage requirements and cloud masking were discussed with T. Nakajima. We agreed to forgo the use of the 1.64 μm channel. The 3.7 channel and ancillary data will be used to assist in detecting clouds over snow.

Algorithm Status

ATSK1, ATSK2 were submitted and accepted by EORC on November 1997. Initial check-out was finished in January 1998.

Version 1 of the GLI cloud mask was delivered on November 26 to NASDA. We developed a version of the code that operates on MAS data, a NASA instrument that flies on the ER-2 and has many

similar channels as the GLI. This code is available of GLI scientists. We worked with Dr. Junichi Inoue as he tested this code. Static analyzing the source programs was error free, compiling and linking was also completed without errors. The output cloud mask data calculated in EORC were coincident with the one delivered for both daytime and nighttime cases.

Algorithm Theoretical Basis Document has been written which describes the GLI cloud mask and is attached.

Activities Planned for the Next Reporting Period:

- validating the GLI cloud mask through comparison with lidar observations,
- comparison of GLI mask with MODIS cloud mask using MAS observations,
- determine threshold optical depth detected by the GLI mask,
- define the conditions for which the cloud mask algorithm will not be executed,
- preparation of the next version of the GLI cloud mask,
- assessment of using a clear sky radiance composite map, and
- attend the September GLI workshop.

Summary of Percent Completion

The preliminary cloud/clear detection algorithm has been developed and delivered to EORC. Revisions and validation of the algorithm need to be conducted during the next period. We are approximately 50% complete with the project.

Steve Ackerman
SSEC/CIMSS/AOS
1225 W. Dayton Street
University of Wisconsin-Madison
Madison, WI 53706
stevea@ssec.wisc.edu
Phone: 608-263-3647
Fax: 608-262-5974

DISCRIMINATING CLEAR-SKY FROM CLOUD WITH GLI

Steve Ackerman

(In collaboration with the MODIS Cloud Mask Team)

Cooperative Institute for Meteorological Satellite Studies, University of Wisconsin - Madison

Version 1.0

June 1997

TABLE OF CONTENTS

1.0 Introduction

Clouds are generally characterized by higher reflectance and lower temperature than the underlying earth surface. As such, simple visible and infrared window threshold approaches offer considerable skill in cloud detection. However, there are many surface conditions when this characterization of clouds is inappropriate, most notably over snow and ice. Additionally, some cloud types such as thin cirrus, low stratus at night, and small cumulus are difficult to detect because of insufficient contrast with the surface radiance. Cloud edges cause further difficulty since the instrument field of view will not always be completely cloudy or clear.

The 36 channel Global Imager (GLI) offers the opportunity for multispectral approaches to cloud detection so that many of these concerns can be mitigated. This document describes the approach and algorithms for detecting clouds using GLI observations. The algorithms have been drafted in close collaboration with members of the MODIS Science Team. A cloud mask algorithm that incorporates MAS observations to simulate the GLI cloud mask is available to the science team to the GLI masking approach. Section 2 gives an overview of the masking approach. The individual spectral tests are discussed in Section 3, and Section 4 discusses some practical applications.

2.0 Overview

2.1 Objective

The GLI cloud mask will indicate whether a given view of the earth surface is unobstructed by clouds or optically thick aerosol, and whether that clear scene is contaminated by a shadow. The cloud mask will be generated at 1 km resolution. Input to the cloud mask algorithm is assumed to be calibrated and navigated level 1B radiance data. Additionally, the GLI data are assumed to be meeting specification. The cloud mask will be determined for good data only. Incomplete or bad radiometric data will create holes in the cloud mask.

Several points need to be made regarding the approach to the GLI cloud mask presented in this document.

(1) This is version 1.0.

(2) The cloud mask algorithm assumes that calibrated, quality controlled data are the input and a cloud mask is the output.

(3) While the current version relies heavily on the MODIS cloud mask there are notable differences between the two approaches: the output of the GLI cloud mask is 16 bits (the MODIS is 48 bits) and is run on 1 km pixels only.

The snow bit in the cloud mask output indicates a processing path in the current algorithm and should not be considered the final indicator of this product. This is the first step in distinguishing cloud from snow. In certain heavy aerosol loading situations (e.g., dust storms, volcanic eruptions and forest fires) particular tests may flag the aerosol laden atmosphere as cloudy. An aerosol bit has initially been included in the mask to indicate fields of view that are potentially contaminated with optically thick aerosol.

In the cloud masking with GLI, there are operational constraints to consider. These constraints are driven by the need to process GLI data in a timely fashion.

◊ CPU Constraint: Many algorithms must first determine if the pixel observation is cloudy or clear. A single cloud mask for GLI exists to avoid duplication in the many GLI algorithms. Thus, the cloud mask algorithm lies at the top of the data processing chain and must be versatile enough to satisfy the needs of many applications. The clear-sky determination algorithm must run in real time, limiting the use of CPU-intensive algorithms.

- ◊ Output File Size Constraint: Storage requirements are also a concern. The current cloud mask is more than a yes/no decision. The 16 bits of the mask include an indication of the likelihood that the pixel is contaminated with cloud. It also includes ancillary information regarding the processing path and the results from individual tests and other useful information (e.g., land/sea tag). In processing applications, one need not process all the bits of the mask. An algorithm can make use of only the first 8 bits of the mask if that is appropriate. The current mask requires approximately 1.5 gigabytes of storage per day.
- ◊ Comprehension: Because there are many users of the cloud mask, it is important that the mask not only provide enough information to be widely used but is also easily understood. To intelligently interpret the output from this algorithm, it is important to have the algorithm simple in concept but effective in its application.

2.2 *Background*

Development of the GLI cloud mask algorithm benefits from previous work to characterize global cloud cover using satellite observations. It builds on the current MODIS cloud masking algorithm. Other approaches that have influenced the development of the MODIS/GLI mask are briefly discused in this section. The International Satellite Cloud Climatology Project (ISCCP) has developed cloud detection schemes using visible and infrared window radiances. The AVHRR (Advanced Very High Resolution Radiometer) Processing scheme Over cLoud Land and Ocean (APOLLO) cloud detection algorithm uses the five visible and infrared channels of the AVHRR. The NOAA Cloud Advanced Very High Resolution Radiometer (CLAVR) also uses a series of spectral and spatial variability tests to detect a cloud. CO_2 slicing characterizes global high cloud cover, including thin cirrus, using infrared radiances in the carbon dioxide sensitive portion of the spectrum. Additionally, spatial coherence of infrared radiances in cloudy and clear skies has been used successfully in regional cloud studies. The following paragraphs briefly summarize some of these prior approaches to cloud detection.

The International Satellite Cloud Climatology Project (ISCCP) cloud masking algorithm is described by Rossow (1989, 1993), Rossow et al. (1989), Seze and Rossow (1991) and Rossow and Gardner (1993). Only two channels are used in cloud detection, the narrowband visible (0.6

μm) and the infrared window (11 μm). Each observed radiance value is compared with its corresponding clear-sky Composite value. Clouds are detected only when they alter the radiances by more than the uncertainty in the clear values. In this way the "threshold" for cloud detection is the magnitude of the uncertainty in the clear radiance estimates.

The ISCCP algorithm is based on the premise that the observed visible and infrared radiances are caused by only two types of conditions, *cloudy* and *clear*, and that the ranges of radiances and their variability that are associated with these two conditions do not overlap (Rossow and Garder 1993). As a result, the algorithm is based upon thresholds; a pixel is classified as cloudy only if at least one radiance value is distinct from the inferred clear value by an amount larger than the uncertainty in that clear threshold. The uncertainty can be caused both by measurement errors and by natural variability. This algorithm is constructed to be cloud-conservative, minimizing false cloud detections but missing clouds that resemble clear conditions.

The ISCCP cloud-detection algorithm consists of five steps (Rossow and Garder 1993): (1) space contrast test on a single infrared image; (2) time contrast test on three consecutive infrared images at constant diurnal phase; (3) cumulation of space/time statistics for infrared and visible images; (4) construction of clear-sky composites for infrared and visible every 5 days at each diurnal phase and location; and (5) radiance threshold for infrared and visible for each pixel.

The AVHRR Processing scheme Over cLoud Land and Ocean (APOLLO) is discussed in detail by Saunders and Kriebel (1988), Kriebel et al. (1989) and Gesell (1989). The scheme uses AVHRR channels 1 through 5 at full spatial resolution, nominally 1.1 km at nadir. The 5 spectral bandpasses are approximately 0.58-0.68 μm, 0.72-1.10 μm, 3.55-3.93 μm, 10.3-11.3 μm, and 11.5-12.5 μm. The technique is based on 5 threshold tests. A pixel is called cloudy if it is brighter or colder than a threshold, if the reflectance ratio of channels 2 to 1 is between 0.7 and 1.1, if the temperature difference between channel 4 and 5 is above a threshold, and if the spatial uniformity over ocean is greater than a threshold (Kriebel and Saunders, 1989). These tests distinguish between cloud free and cloudy pixels. A pixel is defined as cloud free if the multispectral data have values below the threshold for each test. The pixel is defined as cloud contaminated if it fails any single test, thus it is cloud conservative. Two of those tests are then used with different thresholds to identify fully cloudy pixels from the cloud contaminated ones.

The NOAA CLAVR algorithm (Phase I) uses all five channels of AVHRR (0.63, 0.86, 3.7, 11.0, 12.0 μm) to derive a global cloud mask (Stowe et al. 1991). It examines multispectral information, channel differences, and spatial differences and then employs a series of sequential decision tree tests. Cloud free, mixed (variable cloudy), and cloudy regions are identified for 2×2 global area coverage (GAC) pixel (4 km resolution) arrays. If all four pixels in the array fail all the cloud tests, then the array is labeled as cloud-free (0% cloudy). If all four pixels satisfy just one of the cloud tests, then the array is labeled as 100% cloudy. If 1 to 3 pixels satisfy a cloud test, then the array is labeled as mixed and assigned an arbitrary value of 50% cloudy. If all four pixels of a mixed or cloudy array satisfy a clear-restorer test (required for snow or ice, ocean specula reflection, and bright desert surfaces) then the pixel array is re-classified as "restored-clear" (0% cloudy). The set of cloud tests is subdivided into daytime ocean scenes, daytime land scenes, nighttime ocean scenes and nighttime land scenes.

Subsequent phases of CLAVR, now under development, will use dynamic thresholds predicted from the angular pattern observed from the clear-sky radiance statistics of the previous 9-day repeat cycle of the NOAA satellite for a mapped one degree equal area grid cell (Stowe et al. 1994). As a further modification, CLAVR will include pixel by pixel classification based upon different threshold tests to separate clear from cloud contaminated pixels and to separate cloud contaminated pixels into partial and overcast cover. Cloud contaminated pixels are radiatively "typed" as belonging to low stratus, thin cirrus, and deep convective cloud systems. A fourth type indicates all other clouds, including mixed level clouds.

Many algorithms have also been developed for cloud clearing of the TIROS-N Operational Vertical Sounder (TOVS). For example, the fifth version of the International TOVS Processing Package (ITPP-5, Smith et al. 1993), uses collocated AVHRR and HIRS/2 to cloud clear the HIRS/2 footprints. A 3×3 retrieval box of collocated AVHRR and HIRS/2 are used to determine the warm, overall and cold scenes. A scene, or HIRS/2 field of view, is classified as cloudy if any of the following conditions are meet:

1. The average AVHRR $BT_{3.7}$ or the warm signal exceeds the average AVHRR BT_{11} warm signal;
2. The skin temperature as derived from the AVHRR is more than 10°C colder than the initial guess surface temperature;

3. The average albedo for the warm HIRS/2 footprint in either of the AVHRR solar channels is greater than 25% (day tests);
4. The albedo in the HIRS visible channel (channel 20) is larger than 25% (day test);
5. The average AVHRR $BT_{3.7}$ for the warm scene is more than 4°C warmer than the skin temperature as derived by the AVHRR (night test);
6. The average HIRS/2 $BT_{3.7}$ for the warm scene is more than 4°C warmer than the skin temperature as derived by the HIRS/2 (night test); or
7. Skin temperatures derived from the AVHRRR and HIRS/2 differ by more than 2°C.

If a HIRS/2 footprint is determined cloudy, further tests are executed to determine the nature of the cloud cover. Other TOVS cloud clearing approaches (Rizzi et al. 1994) are based on the N* approach developed by Smith (1968).

Operational GOES products by NESDIS also require cloud detection and are referred to as "cloud clearing." In this application, an array of n×n contiguous pixels is categorized as either *clear*, *cloudy* or *unusable*. The *clear* arrays are subcategorized as *truly clear* and *clear/cloudy*. In an approach similar to the ITPP-5 method, clear conditions are determined based on brightness thresholds, difference thresholds, and comparison of observations with first guess profiles.

The above algorithms are noted as they have been incorporated into current global cloud climatologies. The above cloud detection schemes have been run in an operational mode over long time periods and thus faced some of the constraints of the GLI cloud mask algorithm. Many other studies (see the reference list) of cloud detection influenced this draft of the GLI mask. The GLI cloud mask algorithm builds on this work, and current work beginning developed for MODIS.

2.3 GLI Characteristics

The GLI bands used in the version 1.0 of the cloud mask algorithm are:

Band	Wavelength (μm)	Used in Cloud Mask	
8	0.55	Y	thick clouds
13	0.68	Y	clouds
19	0.88	Y	low clouds
26	1.24	Y	snow, clouds
27	1.38	Y	thin cirrus
28	1.64	Y	snow, cloud
30	3.7	Y	window
31	6.7	Y	high moisture
34	8.6	Y	mid moisture
35	10.8	Y	window
36	12.0	Y	low moisture

In preparation for a GLI day-1 cloud mask product, observations from the MODIS Airborne Simulator (MAS) (King et al. 1996), AVHRR, and the HIRS/2 are being used to develop a multispectral cloud mask algorithm. The AVHRR and HIRS/2 instruments fly on the NOAA polar orbiting satellite, while the MAS flies onboard NASA's high altitude ER-2 aircraft collecting 50 m resolution data across a 37 km swath. The multispectral nature of MAS enhances the cloud detection capability, especially for highly varying surface, atmospheric, and cloud characteristics present on the global scale.

A three month global data set of collocated AVHRR and HIRS/2 observations is also being used to develop and test the cloud masking algorithm globally. The real-time algorithm (Frey et al. 1996) collocated and analyzed the AVHRR and HIRS/2 observations and is referred to as CHAPS (Collocated HIRS/2 and AVHRR Processing Scheme). This collocated data set has the advantage of containing many IR observations that are similar to the planned GLI channels. The CHAPS data are used to assist in setting infrared thresholds for cloudy conditions over water. AVHRR GAC scenes are also being used to gain experience with global processing and the development and use of clear-sky radiance maps.

AVHRR LAC scenes are also being used to familiarize the algorithm with handling large data sets with a 1 km spatial resolution. These LAC data are also used to gain experience with incorporating satellite observations with the 1 km land/sea files and ecosystem maps.

The basic data sets currently being used to develop the cloud mask algorithm are listed below, as well as brief descriptions of the advantages and disadvantages of each. Examples are provided later.

Data Set	Advantages	Disadvantages
AVHRR LAC	Similar spatial resolution; Readily available	5 Channels; No global coverage
AVHRR GAC	Global coverage; Readily available	5 Channels; 4 km footprint
Collocated HIRS/AVHRR	Many GLI-like channels; Collocation of smaller pixels within larger footprint	Large HIRS/2 FOV; Gaps between HIRS footprints
MAS (50 channels)	Most GLI like data set; High spatial resolution	No global coverage

2.4 Cloud Mask Inputs and Outputs

The following paragraphs summarize the input and output of the GLI cloud algorithm. Details on the multispectral single field of view (FOV) and spatial variability algorithms are found in the algorithm description section. As indicated earlier, input to the cloud mask algorithm is assumed to be calibrated and navigated level 1B radiance data in channels 8, 13, 19, 26, 27, 28, 30, 31, 34, 35, and 36. Additional channels may be incorporated in the next version of the GLI cloud mask. Incomplete or bad radiometric data will create holes in the cloud mask. Additionally, the cloud mask requires several ancillary data inputs:

* sun angle, azimuthal angle, and viewing angle: obtained from MOD03 (geolocation fields),
* land/water map at 1 km resolution: currently the land/water map is provided by the EDC,
* ecosystems: 1 km map of ecosystems is desired; The Olson map of ecosystems at 10-minute resolution is used for global processing. Over North America the 1 km ecosystem provided by Tom Loveland is used,
* surface temperatures (sea and land) at best available resolution,
* snow map at the best available resolution.

The best available ancillary data will be used for the day-1 GLI cloud mask. However, it is expected that several GLI investigator products will improve upon these ancillary data, so an evolutionary development of the cloud mask is envisioned.

The output of the GLI cloud mask algorithm will be a 16 bit word for each field of view. The mask includes information about the processing path the masking took (e.g., land or ocean) and whether a view of the surface is obstructed. We recognize that a potentially large number of applications will use the cloud mask. Some algorithms will be more tolerant of cloud contamination than others. For example, some algorithms may apply a correction to account for the radiative effects of a thin cloud. In addition, certain algorithms may use spectral channels that are more sensitive to the presence of clouds than others.

The boundary between defining a pixel as cloudy or clear is sometimes ambiguous. For example, a pixel may be partly cloudy, or a pixel may appear as cloudy in one spectral channel and appear cloud free at a different wavelength. Figure 1 shows three spectral images of a subvisual

contrail taken from the MODIS Airborne Simulator (MAS). The left most panel is a MAS image in the 0.66 μm channel, a spectral channel typical of many satellites and commonly used by land surface classifications such as the NDVI. The contrail is not discernible in this image and scattering effects of the radiation may be accounted for in an appropriate atmospheric correction algorithm. The right most panel is a MAS 11 μm image (dark is cold, light is warm). Evidence of a contrail lingers though it would be difficult to justify its existence without the aid of the center panel — an image of the 1.88 μm channel. The 1.88 μm spectral channel is near a strong water vapor absorption band and, during the day, is extremely sensitive to the presence of high level clouds. While the contrail seems to have little impact on visible reflectances, its effect in the infrared window is enough to affect the retrievals of surface temperature. In this type of scene, the cloud mask needs to provide enough information to be useful to both visible and infrared applications. The 1.88 μm spectral channel on MAS is expected to exhibit similar characteristics to the 1.38 μm spectral channel to be available on GLI.

To accommodate a wide variety of applications, the mask is more than a simple yes/no decision (though bit 1 alone could be used to represent a single bit cloud mask). The cloud mask includes 4 levels of 'confidence' with regard to whether a pixel is thought to be clear (bits 1 and 2)[1] as well as the results from different spectral tests. The bit structure of the cloud mask is:

---

[1] In this document, representations of bit fields are ordered from right to left. Bit 0, or the right-most bit, is the least significant.

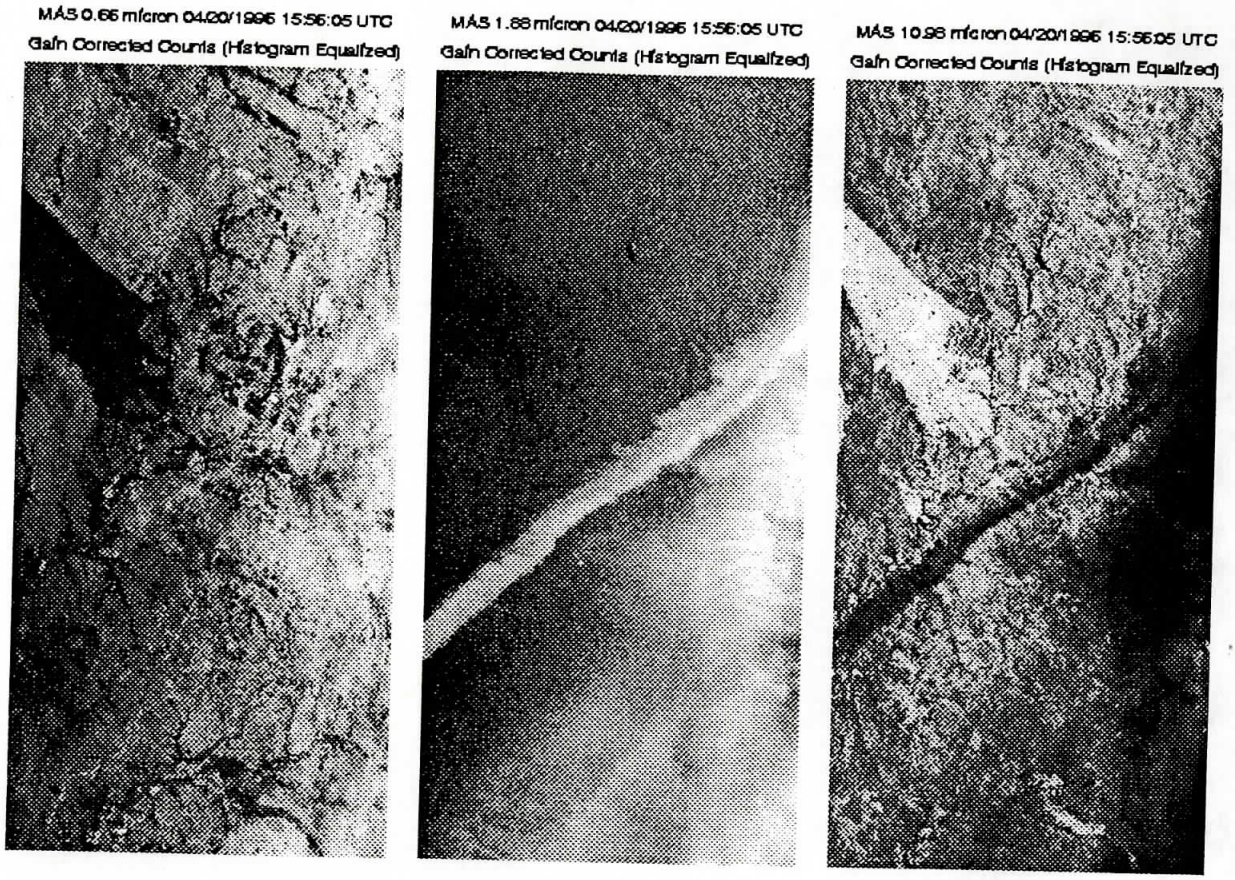

Figure 1. Three spectral images (0.66, 1.88 and 11 μm) taken from the MAS during the SUCCESS experiment (20 April 1996). In the 11 μm image, dark is cold.

16 BIT GLI CLOUD MASK FILE SPECIFICATION		
BIT FIELD	**DESCRIPTION KEY**	**RESULT**
0-1	Unobstructed FOV Quality Flag	00 = cloudy 01 = probably clear 10 = confident clear 11 = high confidence clear
PROCESSING PATH FLAGS		
2	Day / Night Flag	0 = Night / 1 = Day
3	Sun glint Flag	0 = Yes / 1 = No
4	Snow / Ice Background Flag	0 = Yes/ 1 = No
5-6	Land / Water Flag	00 = Water 01 = Coastal 10 = Desert 11 = Land
ADDITIONAL FLAGS		
7	Non-cloud obstruction Flag (heavy aerosol)	0 = Yes / 1 = No
8	Thin Cirrus Detected (solar)	0 = Yes / 1 = No
9	Shadow Detected	0 = Yes / 1 = No
1-km CLOUD FLAGS		
10	Result from Group I tests	0 = Yes / 1 = No
12	Result from Group II tests	0 = Yes / 1 = No
13	Result from Group III tests	0 = Yes / 1 = No
14	Result from Group IV tests	0 = Yes / 1 = No
15	Result from Group V tests	0 = Yes / 1 = No

2.4.1 Processing Path (bits 2-6)

These input bits describe the processing path taken by the cloud mask algorithm. They are important bits for the interpretation of the cloud mask results.

Bit 2 - Day / Night Flag

A combination of solar zenith angle and instrument mode (day or night mode) at the pixel latitude and longitude at the time of the observations is used to determine if a daytime or nighttime cloud masking algorithm should be applied. Daytime algorithms, which include solar reflectance data, are constrained to solar zenith angles less than 85°. If this bit is set to 1, daytime algorithms were executed.

Bit 3 - Sun glint Flag

Sun glint processing path is taken when the reflected sun angle, θ_r, lies between 0° and approximately 36°, where

$$\cos\theta_r = \sin\theta \sin\theta_{\square} \cos\psi + \cos\theta\cos\theta \qquad (1)$$

where θ is the solar zenith angle, θ is the viewing zenith angle, and ψ is the azimuthal angle. Sun glint is also a function of surface wind and sea state.

Bit 4 - Snow / Ice Background Flag

Certain cloud detection tests (e.g., visible reflectance tests) are applied differently in the presence of snow or ice. This bit is set to a value of 0 when the cloud mask processing algorithm assumes that snow is present.

Bits 5 and 6 - Land / Water Background Flag

Bits 5 and 6 of the cloud mask output file contain information concerning the processing path taken through the algorithm. There are four possible surface type processing paths: land, water, desert, or coast. Naturally, there are times when more than one of these flags could apply to a pixel. For example, the northwest coast of the African continent could be simultaneously characterized as coast, land, and desert. In such cases, we choose to output the flag which indicates the most important characteristic for the cloud masking process. The flag precedence will be as follows: coast, desert, land or water.

Thresholds for the spectral tests are a function of surface background, land and water being the two most obvious. Therefore, each pixel will be tagged as being land or water. The 1 km United States Geological Survey (USGS) global land/water mask is currently used for this determination (available from USGS at http://edcwww.cr.usgs.gov/landdaac/1KM/1kmhomepage.html).

Some cloud detection algorithms are also ecosystem dependent. Thus, an ecosystem will be determined for each land pixel. Over North America the current version of the cloud mask uses the 1 km ecosystem map of Loveland, available from EDC. Global applications currently use the 10-minute resolution Olson World Ecosystem map.

As improved ancillary data bases become available, they will be incorporated into the GLI cloud mask. The at launch product will make use of the best available land/sea and ecosystem map with a 1 km spatial resolution.

2.4.2 Output (bits 0,1 and 7-15)

This section gives a brief description of the meaning of the output bits.

Bits 0-1 - Unobstructed FOV Quality Flag[2]

Confidence flags convey strength of conviction in the outcome of the cloud mask algorithm tests for a given FOV. When performing spectral tests, as one approaches a threshold limit, the certainty or confidence in the outcome is reduced. Therefore, a confidence flag for each individual test, based upon proximity to the threshold value, is assigned and used to work towards a final quality flag determination for the FOV. The current scheme applies a linear interpolation between a low confidence clear threshold (0% confidence of clear) and high confidence clear threshold (100% confidence clear) for each spectral test.

---

[2] There are conditions for which the cloud mask algorithm will not be executed. For example, if all the radiance values used in the cloud masking are deemed bad, then masking cannot be undertaken. Conditions (e.g., missing spectral observations) for which the cloud mask algorithm will not be executed will be set for Version 2 of the cloud mask code. Bad radiances are flagged in the data input stream. Unlike the MODIS cloud mask, an execution bit is not specified in the GLI cloud mask.

The final determination is a combination of the confidences of all applied tests. This determination will dictate whether additional testing (using spatial variability tests) is warranted to improve the confidence. The final cloud mask determination will be clear or cloudy with a confidence level associated with it. This approach quantifies our confidence in the derived cloud mask for a given pixel.

Bit 7 - Non-cloud Obstruction

Smoke from forest fires, dust storms over deserts, and other aerosols that result in obstructing the FOV between the surface and the satellite may be flagged as "cloud." The aerosol obstruction bit will be set to on (a value of 0) if simple spectral tests indicate the possible presence of aerosols. This bit is not an aerosol product; rather, if the bit is set to zero, then the instrument may be viewing an aerosol laden atmosphere. An example of such an aerosol test is presented in Section 3.

Bit 8 - Thin Cirrus (near infrared)

GLI includes a unique spectral channel — 1.38 μm — specifically included for the detection of thin cirrus. Land and sea surface retrieval algorithms may attempt to correct the observed radiances for the effects of thin cirrus. The definition of *thin* will be determined in collaboration with the GLI Atmosphere, Land and Ocean groups. This test is discussed in Section 3 If this bit is set to 0, thin cirrus was detected using this channel.

Bit 9 - Shadow bit

Some land retrieval products are as sensitive to the presence of shadows as they are to contamination by thin clouds. If there is a need for a shadow bit, then one will be included in the GLI cloud mask. The GLI cloud masking algorithm checks for the presence of a shadow whenever bits 0 and 1 are greater than 00. Though much work remains, section 3.2.6 discusses the shadow detection algorithm. If this bit is set to zero, a shadow was detected using spectral tests. If bits 0 and 1 are 11 (low confidence clear), tests will be run to discern if a shadow from a high cloud is being cast on a lower cloud. In such a case is detected, this bit is set to zero.

Bits 10 - Thin Cirrus (infrared)

It is likely that some IR algorithms will be insensitive to thin cirrus flagged by the GLI 1.38 μm channel. In addition, this 1.38 μm channel is not available during the night. This second thin cirrus bit indicates that IR tests detect a thin cirrus cloud. The results are independent of the results of bit 8. The definition of *thin* in the infrared will be determined in collaboration with the GLI Atmosphere, Land and Ocean groups. This test is discussed in Section 3. If this bit is set to 0, thin cirrus was detected using infrared channels.

Bits 11 through 15 - 1 km Cloud Mask

These 5 bits represent the results of tests that make use of the 1 km observations. Each group of tests is discussed in the next section. These bits are used for interpretation of the cloud mask output.

3.0 Algorithm Description

The theoretical basis of the algorithms and practical considerations are contained in this section. For nomenclature, we shall denote the satellite measured solar reflectance as R, and refer to the infrared radiance as brightness temperature (equivalent blackbody temperature using the Planck function) denoted as BT. Subscripts refer to the wavelength at which the measurement is made.

The strategy for this cloud mask algorithm is to start with single pixel (1000 m field of view) tests. Many of the single pixel tests rely on radiance (temperature) thresholds in the infrared and reflectance thresholds in the solar. These thresholds vary with surface emissivity, with atmospheric moisture and aerosol content, and with GLI viewing scan angle. A large part of the algorithm preparation will be to characterize the different situations and the different thresholds.

3.1. Confidence Flags

Most of the single pixel tests that are discussed in following sections rely on thresholds. Thresholds are never global. There are always exceptions. For example, the ratio of reflectance at 0.86 to 0.66 μm identifies cloud for values in the range $0.9 < R_{.87}/R_{.66} < 1.1$. It seems unrealistic to label a pixel with $R_{.87}/R_{.66} = 1.09$ as cloudy, and a neighboring pixel with the ratio of 1.11 as non-cloudy. Rather, as one approaches the threshold limits, the certainty or confidence in the labeling becomes more and more uncertain. An individual confidence flag is assigned to each single pixel test and is a function of how close the observation is to the thresholds. The individual confidence flags are combined to produce the final cloud mask flag for the output file (bits 1 and 2).

Each threshold determination will be pass, conditional pass, or fail along with a confidence assessment (given in a percent). Conditional pass will involve those radiances that fall within an uncertainty region of the threshold. The uncertainty will be a measure of instrument noise in that channel and the magnitude of the correction that was necessary due to surface spectral radiative properties, as well as atmospheric moisture and/or aerosol reflection contributions. The individual confidence flag will indicate a confidence level for each single pixel test result. The initial FOV obstruction determination is an amalgamation of all confidence flags and single pixel test results

This determination will dictate whether additional testing (e.g., spatial uniformity tests) is warranted to improve the confidence. The final cloud mask determination (bits 1 and 2) is a clear-sky confidence with one of four levels associated with it: definitely clear, probably clear, possibly clear and definitely obstructed. This approach quantifies our confidence in the derived cloud mask for a given pixel. This section describes the method of assigning a confidence to a given spectral test.

Many cloud detection schemes have a single threshold for a given test. For example, if the visible reflectance over the ocean is greater than 6% then the pixel is set to cloudy. The cloud masking is designed to provide information on how much confidence a user can place on the result. Each test is assigned a value between 0 and 1 representing increasing confidence in clear-sky conditions. Figure 2 is a graphical representation of how a confidence level is assigned for a spectral test. The abscissa represents the observation and the ordinate the clear-sky confidence level. In this test, an observation greater than a value of γ is determined to be a high confidence clear scene and assigned a value of 1. An observation with a value less than α is cloudy and assigned a confidence level of 0. These high confidence clear and cloud thresholds, γ and α respectively, are determined from observations and/or theoretical simulations.

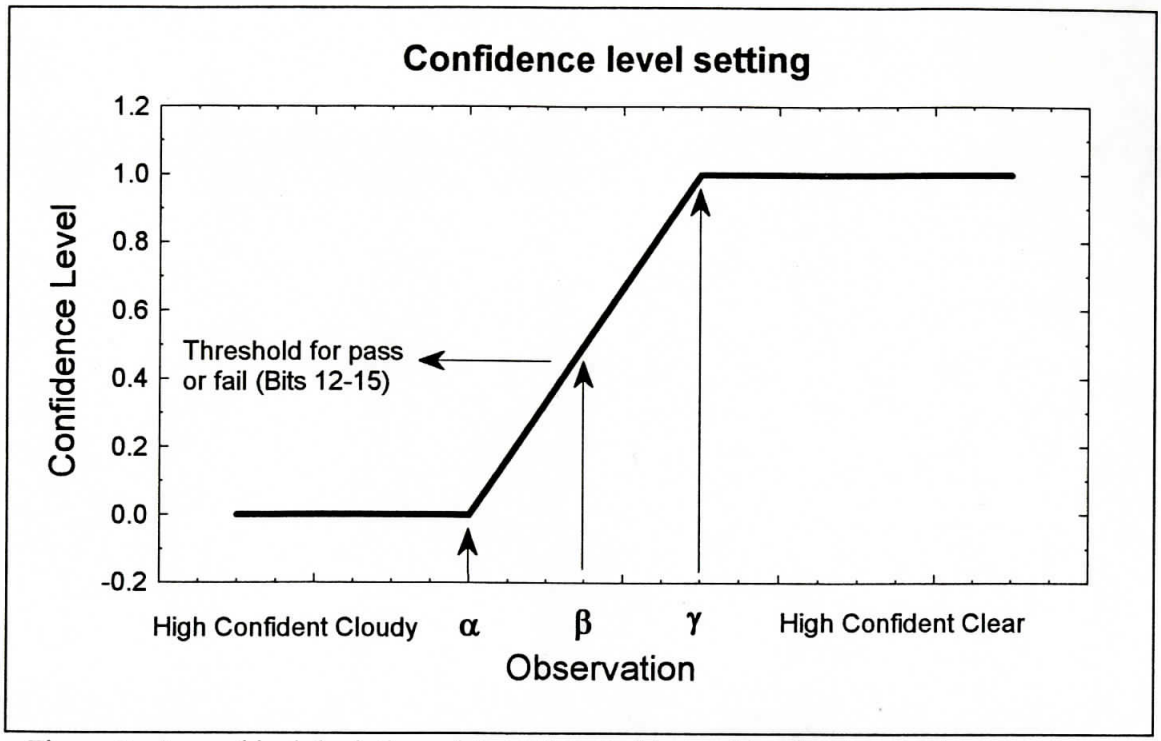

Figure 2. A graphical depiction of three thresholds used in cloud screening.

Values between α and γ are assigned a value between 0 and 1 (or 1 and 0). Assignment is based on a linear function. We have experimented with assigning confidence values based on S-functions:

$$S(x;\alpha,\beta,\gamma)=\begin{cases}0 & \text{for } x\le\alpha\\ 2\left(\dfrac{x-\alpha}{\gamma-\alpha}\right)^2 & \text{for } \alpha\le x\le\beta\\ 1-2\left(\dfrac{x-\alpha}{\gamma-\alpha}\right)^2 & \text{for } \beta\le x\le\gamma\\ 1 & \text{for } x\ge\gamma\end{cases} \tag{2}$$

The S-function is quadratic between the points α and γ. If the '2' exponent in the above equation is replaced with a 1, then the S-function becomes linear. Experiments indicate that changing between a quadratic and linear function primarily affects cloud masking at the edge of cloud systems. For simplicity we have stayed with the linear function.

In the final cloud mask only four levels of confidence are provided. Numerical values are assigned to each of these four confidence levels, 0.99 confidence of clear, 0.95 0.66 and less than 0.66 These numerical values are set based on how close the observed value is to a set of thresholds. A description of how the final confidence level is determined is given in section 3.2.8.

3.2 *Theoretical Description of Cloud Detection*

This section discusses the physics of detecting clouds using multispectral radiances from a given field of view (FOV) or an array of FOVs, presents the application with GLI data, and indicates various problem areas.

3.2.1 Infrared Brightness Temperature Thresholds and Difference (BTD) Tests

The azimuthally averaged form of the infrared radiative transfer equation:

$$\mu \frac{\mathrm{d}I(\delta,\mu)}{\mathrm{d}\delta} = I(\delta,\mu) - (1-\omega_{\circ})B(T) - \frac{\omega_{\circ}}{2}\int_{-1}^{1} P(\delta,\mu,\mu')\, I(\delta,\mu')\,\mathrm{d}\mu' \qquad (3)$$

In addition to atmospheric structure, which determines *B(T)*, the parameters describing the transfer of radiation through the atmosphere are the single scattering albedo, $\omega_{\square} = \sigma_{sca}/\sigma_{ext}$, which ranges between 1 for a non-absorbing medium and 0 for a medium that absorbs and does not scatter energy, the optical depth, δ, and the Phase function, $P(\mu,\mu')$, which describes the direction of the scattered energy.

To gain insight on the issues of detecting clouds using IR observations from a satellite, it is useful to first consider the two-stream solution to equation (3). Using the discreet-ordinates approach (Liou, 1973; Stamnes and Swanson, 1981), the solution for the upward radiance out the top of a uniform single cloud layer is:

$$I_{obs} = M_{-}L_{-}\exp(-k\delta) + M_{+}L_{+} + B(T_c) \qquad (4)$$

where

$$L_{+} = \frac{1}{2}\left[\frac{I\downarrow + I\uparrow - 2B(T_c)}{M_{+}e^{-k\delta} + M_{-}} + \frac{I\downarrow + I\uparrow}{M_{+}e^{-k\delta} + M_{-}}\right] \qquad (5)$$

$$L_{-} = \frac{1}{2}\left[\frac{I\downarrow + I\uparrow - 2B(T_c)}{M_{+}e^{-k\delta} + M_{-}} + \frac{I\downarrow - I\uparrow}{M_{+}e^{-k\delta} - M_{-}}\right] \qquad (6)$$

$$M_{\pm} = \frac{1}{1 \pm k}\left(\omega_{\circ} \mathrm{m}\, \omega_{\circ} g(1-\omega_{\circ})\frac{1}{k}\right) \tag{7}$$

$$k = \left[(1-\omega_{\circ})(1-\omega_{\circ} g)\right]^{\frac{1}{2}} \tag{8}$$

$I\downarrow$ is the downward radiance (assumed isotropic) incident on the top of the cloud layer and $I\uparrow$ is the upward radiance at the base of the layer and g is the asymmetry parameter. T_c is a representative temperature of the cloud layer.

The challenge in cloud masking is detecting thin clouds. Assuming a thin cloud layer, the effective transmittance (ratio of the radiance exiting the layer to that incident on the base) is derived from equation (4) by expanding the exponential. The effective transmittance is a function of the ratio of $I\downarrow/I\uparrow$ and $B(T_c)/I\uparrow$. Using atmospheric window regions for cloud detection minimizes the $I\downarrow/I\uparrow$ term and maximizes the $B(T_c)/I\uparrow$ term. Brightness temperature differences between the clear and cloudy sky result because of the non-linearity of the Planck function and because of the spectral variation in the single scattering properties of the cloud. The magnitude of the difference is also a function of the temperature difference between the cloud and underlying atmosphere. Observations of brightness temperature differences at two, or more, wavelengths can help separate the atmospheric signal from the cloud affect.

The anticipation is that the infrared threshold techniques will be very sensitive to thin clouds, given the appropriate characterization of surface emissivity and temperature. For example, with a surface at 300°K and a cloud at 220°K, a cloud with emissivity of 0.01 affects the sensed brightness temperature by 0.5 K. Since the expected noise equivalent temperature of GLI infrared window channel 31 is 0.05 K, the cloud detecting potential of GLI is obviously very good. The presence of a cloud modifies the spectral structure of the radiance of a clear-sky scene depending on cloud microphysical properties (e.g., particle size distribution and shape) and the temperature difference between the cloud and ground. This spectral signature is the physical reasoning behind the brightness temperature difference tests.

Simple BT threshold Test

Several infrared window threshold and temperature difference techniques have been developed. These algorithms are most effective at night for cold clouds over water and must be

used with caution in other situations. The first infrared test to apply over the oceans is a simple threshold test. Over open ocean when the brightness temperature in the 11 μm (BT_{11}) channel (band 31) is less than 270 K, we assume the pixel to fail the clear-sky condition. With reference to Figure 2, the three thresholds over ocean are 267 K, 270 K and 273 K as demonstrated in Figure 3.

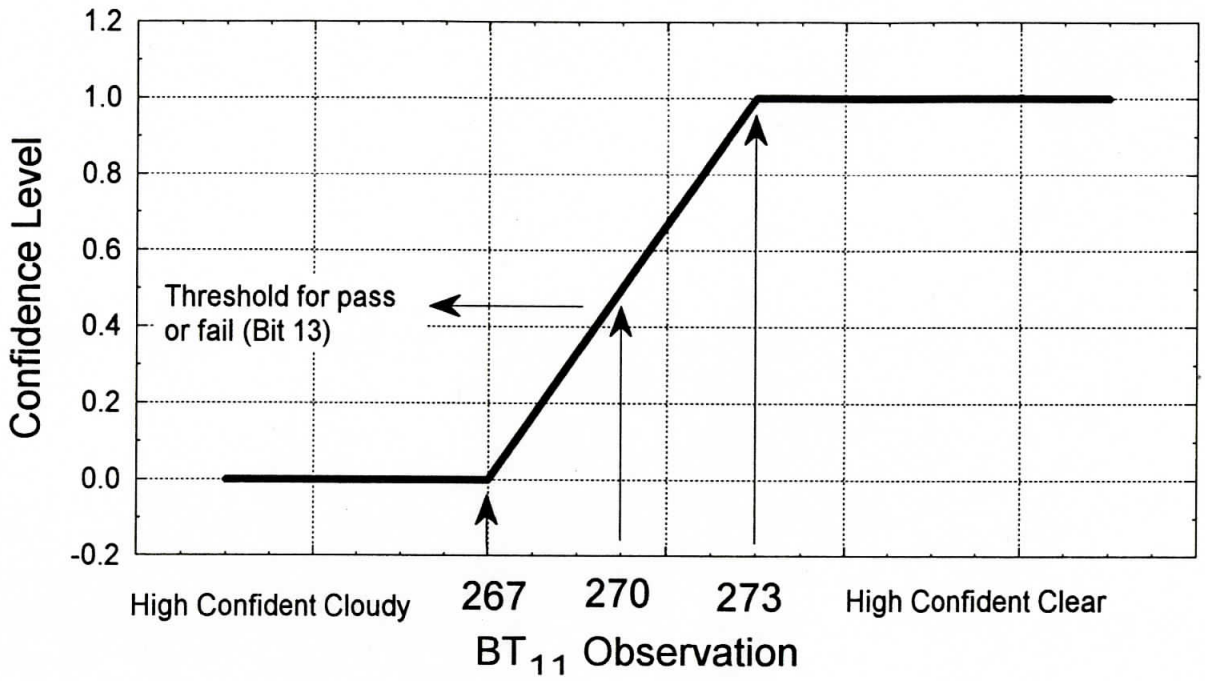

Figure 3. Thresholds for the simple IR window cold cloud test.

Cloud masking over land surface from thermal infrared bands is more difficult than over ocean due to potentially larger variations in surface emittance. Nonetheless, simple thresholds can be established over certain land features. For example, over desert regions we can expect that BT_{11}<273 K denotes cloud. Such simple thresholds will vary with ecosystem, season, and time of day; they are under investigation.

BT_{11} - BT_{12} and $BT_{8.6}$ - BT_{11} Test

As a result of the relative spectral uniformity of surface emittance in the IR, spectral tests within various atmospheric windows (such as bands 34, 35, 36 at 8.6, 10.8, and 12 μm,

respectively) can be used to detect the presence of a cloud. Differences between BT_{11} and BT_{12} are widely used for cloud screening with AVHRR measurements, and this technique is often referred to as the split window technique. Saunders and Kriebel (1988) used BT_{11}-BT_{12} differences to detect cirrus clouds--brightness temperature differences are greater over clouds than clear conditions. Cloud thresholds were set as a function of satellite zenith angle and the BT_{11} brightness temperature. Inoue (1987) also used BT_{11}-BT_{12} versus BT_{11} to separate clear from cloudy conditions.

In difference techniques, the measured radiances at two wavelengths are converted to brightness temperatures and subtracted. Because of the wavelength dependence on optical thickness and the non-linear nature of the Planck function (B_λ), the two brightness temperatures are often different.

The basis of the split window and tri-spectral technique for cloud detection lies in the differential water vapor absorption that exists between different window channel (8.6 and 11 μm and 11 and 12 μm) bandwidths. These spectral regions are considered to be part of the atmospheric window, where absorption is relatively weak. Most of the absorption lines are a result of water vapor molecules, with a minimum occurring around 11 μm. Since the absorption is weak, BT_{11} can be corrected for moisture absorption by adding the scaled brightness temperature difference of two spectrally close channels with different water vapor absorption coefficients; the scaling coefficient is a function of the differential water vapor absorption between the two channels. This is the basis for sea surface temperature retrieval.

With a reasonable estimate of the sea surface temperature and total precipitable water one can develop appropriate thresholds for cloudy sky detection. For example;

$$BT_{11} + a_{PW} * (BT_{11}-BT_{12}) < SST \tag{9}$$

or

$$BT_{11} + b_{PW} * (BT_{11}-BT_{8.6}) < SST \tag{10}$$

where a_{PW} and b_{PW} are determined from a lookup table as a function of total precipitable water vapor (PW). This approach has been used operationally for 4 years using 8.6 and 11 μm bandwidths from the NOAA-10 and NOAA-12 and the 11 and 12 μm bandwidths from the NOAA-11, with a coefficient independent of PW (Menzel et al. 1993, Wylie et al. 1994).

To demonstrate this technique with observations, a global data set of collocated AVHRR GAC 11 and 12 μm and HIRS 8.6 and 11 μm scenes were collected and the total column PW was estimated from integrated model mixing ratios to determine a direct regression between PW and the split window thresholds. The regressions were then modified for use with MODIS Airborne Simulator (MAS) bandwidths in TOGA/COARE data sets. Simulations and observations have shown the regression slopes to be consistent with those found for the AHVRR/HIRS clear scenes; however, the intercept values needed adjustment.

A disadvantage of the split window brightness temperature difference (BTD) approach is that water vapor absorption across the window is not linearly dependent on PW, thus second order relationships are sometimes used. The GLI has a unique capability with the measurements at three wavelengths in the window, 8.6, 10.8, and 12 μm. The three spectral regions mentioned are very useful in determination of cloud free atmospheres. Because the index of refraction varies quite markedly over this spectral region for water, ice, and minerals common to many naturally occurring aerosols, the effect on the brightness temperature of each of the spectral regions is different, depending on the absorbing constituent.

A tri-spectral combination of observations at 8.6, 11 and 12 μm was suggested for detecting cloud and cloud properties by Ackerman et al. (1990). Strabala et al. (1994) further explored this technique by utilizing very high spatial-resolution data from the MODIS Airborne Simulator (MAS). The physical premise of the technique is that ice and water vapor absorption peak in opposite halves of the window region; so that positive 8.6 minus 11 μm brightness temperature differences indicate cloud while negative differences, over oceans, indicate clear regions. The relationship between the two brightness temperature differences and clear-sky have also been examined using collocated HIRS and AVHRR GAC global ocean data sets. As the atmospheric moisture increases, $BT_{8.6}$-BT_{11} decreases while BT_{11}-BT_{12} increases.

Based on these observations, a threshold is set for clear-sky conditions. The clear-sky threshold is set for both differences:

$$T8M11=[-1.64805 \ln (PW)] - 3.19767 \quad (11)$$

$$T11M12= (0.488198 PW) - 0.456924 \quad (12)$$

If $BT_{8.6}$-BT_{11} > T8M11 and BT_{11}-BT_{12} > T11M12, then a cloud is assumed.
High confidence clear conditions are

$$BT_{8.6}\text{-}BT_{11} < T8M11 - 0.5 \text{ and } BT_{11}\text{-}BT_{12} > T11M12 - 0.5 \quad (13)$$

and low confidence clear condition is

$$BT_{8.6}\text{-}BT_{11} < T8M11 + 0.5 \text{ and } BT_{11}\text{-}BT_{12} > T11M12 + 0.5 \quad (14)$$

The above conditions assume an estimate of the precipitable water is available. These equations demonstrate that a relationship between T8M11 and T11M12 exists and thus a PW value is not needed, but rather given a value of T8M11, to be a clear pixel requires T11M12 to fall within a certain range of values.

Brightness temperature difference testing can also be applied over land with careful consideration of variation in spectral emittance. For example, BT_{11}-$BT_{8.6}$ has large negative values over daytime desert and is driven to positive differences in the presence of cirrus. Some land regions have an advantage over the ocean regions because of the larger number of surface observations, which include air temperature, and vertical profiles of moisture and temperature. Work on developing brightness temperature difference tests for application over land scenes continues with the MAS observations.

BT_{11} - $BT_{3.7}$ Test

GLI band 30 (3.7 μm) measures radiances in another window region near 3.5-4 μm so that the difference between BT_{11} and $BT_{3.7}$ can also be used to detect the presence of clouds. At night the difference between the brightness temperatures measured in the shortwave (3.7 μm) and in the longwave (11 μm) window regions (BT_{11}-$BT_{3.7}$) can be used to detect partial cloud or thin cloud within the GLI field of view. Small or negative differences are observed only for the case where an opaque scene (such as thick cloud or the surface) fills the field of view of the sensor. Negative differences occur at night over extended clouds due to the lower cloud emissivity at 3.7 μm.

During the daylight hours the difference between BT_{11} and $BT_{3.7}$ becomes large negative because of reflection of solar energy at 3.7 μm. This technique is very successful at detecting low level water clouds. BT_{11}-$BT_{3.7}$ are not applied over deserts during daytime, as bright desert regions with highly variable emissivities tend to be classified incorrectly as cloudy with this test. Experience indicates that the actual thresholds will need to be adjusted for ecosystem type.

Moderate to large differences between BT_{11} and $BT_{3.7}$ result when a non-uniform scene (e.g., broken cloud) is observed. The different spectral responses to a scene of non-uniform temperature is a result of Planck's law. The brightness temperature dependence on the warmer portion of the scene increasing with decreasing wavelength (the shortwave window Planck radiance is proportional to temperature to the thirteenth power, while the longwave dependence is to the fourth power). Differences in the brightness temperatures of the longwave and shortwave channels are small when viewing mostly clear or mostly cloudy scenes; however, for intermediate situations the differences become large (greater than 3°C). The following table lists the thresholds used, which are based on previous studies and our own investigations.

11 - 3.7 μm Low Cloud Test			
Scene Type	Threshold	High confidence clear	Low confidence clear
Day ocean	-8.0K	-6.0K	-10.0K
Night ocean	0.60K	0.50K	0.70K
Day land	-12.0K	-10.0K	-14.0K
Night land	0.60K	0.50K	0.70K
Day polar	-9.0K	-7.0K	-11.0K
Night polar	0.60K	0.50K	0.70K
Desert	-18.0, -3K	>-16, <-5K	<-20, >-1K

Infrared window tests at high latitudes are difficult. Distinguishing clear and cloud regions from satellite IR radiances is a challenging problem due to the cold surface temperatures. Yamanouchi et al. (1987) describe a nighttime polar (Antarctic) cloud/surface discrimination algorithm based upon brightness temperature differences between the AVHRR 3.7 and 11 μm channels and between the 11 and 12 μm channels. Their cloud/surface discrimination algorithm was more effective over water surfaces than over inland snow-covered surfaces. A number of problems arose over inland snow-covered surfaces. First, the temperature contrast between the cloud and snow surface became especially small, leading to a small brightness temperature difference between the two infrared channels. Second, the AVHRR channels are not well-

calibrated at extremely cold temperatures (< 200 K). This latter condition will be minimized using GLI.

$BT_{3.7}$ - BT_{12} Test

This window brightness temperature difference test is applied during the nighttime. This difference is useful for separating thin cirrus and cloud free condition and is relatively insensitive to the amount of water vapor in the atmosphere (Hutchison and Hardy, 1995).

$BT_{6.7}$ and BT_{11} - $BT_{6.7}$

Detection of clouds over polar regions during winter is difficult. Under clear-sky conditions, strong surface radiative temperature inversions often exist over polar regions during winter. Thus, IR channels whose weighting function peaks low in the atmosphere will often have a larger BT than a window channel. For example, $BT_{8.6} > BT_{11}$ in the presence of an inversion. The surface inversion can also be confused with thick cirrus cloud; this can be mitigated by other tests (e.g., the magnitude of BT_{11} or the BT_{11}-BT_{12}). Analysis of BT_{11}-$BT_{6.7}$ has shown large negative difference in winter time over the Antarctic Plateau and Greenland, which may be indicative of a strong surface inversion and thus clear skies (Ackerman 1996). In clear-sky situations, the 6.7 μm radiation measured by satellite instruments is emitted by water vapor in the atmospheric layer between approximately 200 and 500 hPa (Soden and Bretherton 1993; Wu et al. 1993) and has a brightness temperature ($BT_{6.7}$) related to the temperature and moisture in that layer. The 6.7-μm radiation emitted by the surface or low clouds is absorbed in the atmosphere and is not sensed by the satellite instruments. On the other hand, absorption by atmospheric gases is weak at 11-μm. Under clear-sky conditions, the measured 11 μm radiation originates primarily at the surface, with a small contribution by the near-surface atmosphere. Because the surface is normally warmer than the upper troposphere, BT_{11} is normally warmer than 6.7-μm brightness temperature; thus the difference, BT_{11}-$BT_{6.7}$, is normally greater than zero. Large negative differences in BT_{11}-$BT_{6.7}$ (less than -10°K) exist over the Antarctic Plateau and Greenland during their respective winters and are indicative of clear-sky conditions and the existence of strong low-level temperature inversions.

In polar regions, strong surface radiation inversions can develop as a result of longwave energy loss at the surface due to clear-skies and a dry atmosphere. Temperatures over Antarctica near the surface can reach 200 K (Stearns et al. 1993), while the middle troposphere is ~235K. Under such conditions, satellite channels located in strong water vapor absorption bands, such as the 6.7-μm channel, will have a warmer equivalent brightness temperature than the 11-μm window channel. This brightness temperature difference between 11- and 6.7-μm is an asset to detecting cloud-free conditions over elevated surfaces in the polar night (Ackerman 1996). Clouds inhibit the formation of the inversion and obscure the inversion from satellite detection if the IWP is greater than approximately 20 g m^{-2}. A positive difference of BT_{11}-$BT_{6.7}$ is a cloud; differences smaller than -10C are representative of cloud. This test is applied only during the polar winter.

3.2.2 Non-cloud obstruction flag

A heavy aerosol laden atmosphere may result in a low confidence clear scene. Certain simple tests may be constructed that can indicate that the FOV is contaminated with an aerosol and not a cloud. For example, negative values of BT_{11}-BT_{12} are often observed over deserts and can be attributed to the presence of dust storms (Ackerman 1996). Under such conditions, provided BT_{11} is warm, the non-cloud obstruction bit (Bit 7) would be set. The tri-spectral technique may also be used to flag a region as potentially contaminated with volcanic aerosol. These tests are currently under implementation. In addition, this bit may be used to pass information on to the aerosol retrieval algorithm. For example, over oceans it might indicate the passing or failing of a uniformity test.

3.2.3 Near Infrared 1.38 μm Cirrus Test

This is a new approach to cirrus detection suggested by the work of Gao et al. (1993) and is still under development. The GLI band 27 (1.38 μm) will use reflectance thresholds on a per pixel basis to detect the presence of thin cirrus cloud in the upper troposphere under daytime viewing conditions. The strength of this cloud detection channel lies in the strong water vapor absorption in the 1.38 μm region. With sufficient atmospheric water vapor present (estimated to be about 0.4 cm precipitable water) in the beam path, no upwelling reflected radiance from the earth's surface reaches the satellite. Since 0.4 cm is a small atmospheric water content, most of the

earth's surface will indeed be obscured in this channel. With relatively little of the atmosphere's moisture located high in the troposphere, high clouds appear bright; reflectance from low and mid level clouds is partially attenuated by water vapor absorption.

Simple low and high reflectance (normalized by incoming solar at the top of the atmosphere) thresholds will be used to separate thin cirrus from clear and thick (near infrared cloud optical depth > ~ 0.2) cloud scenes. These thresholds will be set initially using a multiple-scattering model with the assumption of no surface reflectance contribution to the satellite observed radiance, i.e., a dark background. Ben-Dor (1994) analyzed a scene from the AVIRIS to demonstrate that thin cirrus detection using 1.38 μm observations may depend on surface elevation, dry atmospheric conditions, and high albedo surface. New injections of volcanic aerosols into the stratosphere may also impact this test.

The MAS 1.88 μm channel is being used as a surrogate to GLI channel 27 to gain experience with defining the thin cirrus bit. If the reflectance lies between the clear-sky threshold and below a thick cloud, then the cirrus bit will be set to 0. We subjectively define a thin cirrus as a cloud that has a small impact on the visible reflectance, enabling atmospheric correction to be applied to retrieve land surface properties (i.e., NDVI). Figure 1 demonstrates the potential utility of the 1.38 μm channel. The three panels are of observations made from the MAS during the SUCCESS field campaign. The MAS has a 1.88 μm channel which, like the 1.38 μm channel is near a strong water vapor absorption band. The panel to the left is a visible image that has been histogram normalized. The right panel is an 11 μm image where dark regions represent cold scenes. The center scene is the 1.88 μm image which clearly shows the presence of contrails that are difficult to see in the 11 μm image and indiscernible in the 0.66 μm image. Given the sensitivity to thin high clouds, the new 1.38 μm channel may detect a much larger cloud coverage than previous satellite algorithms have indicated.

The initial 1.38 μm reflectance thresholds will be based on theoretical simulations and MODIS observations, and will be adjusted using inflight data after GLI is launched.

3.2.4 Infrared Thin Cirrus Test

This second thin cirrus bit indicates that IR tests detect a thin cirrus cloud. This test is independent of the thin cirrus flagged by the GLI 1.38 μm channel. This test will apply brightness temperature differences tests to detect the presence of thin cirrus. The APOLLO scheme tests for the presence of thin cirrus using the split window analysis. Analysis of BT_{11}-BT_{12} and BT_8-BT_{11} is also effective in detecting the presence of thin cirrus clouds.

3.2.5 Detection of Cloud Shadows

The detection of cloud shadows is a problem that has not been addressed adequately in the literature. Clear-sky scenes that are potentially affected by shadows can be theoretically computed given the viewing geometry, solar azimuth and zenith angles, cloud edges distribution and cloud altitude. This approach requires too much CPU to run operationally, and all the information (e.g., cloud altitude) is not available to the cloud mask algorithm. Therefore, as with clouds, solar reflectance tests will be explored for a cloud shadow detection algorithm. Further work in this area has been initiated.

Currently, the cloud masking algorithm checks for shadows whenever a high confident clear scene is identified. Shadow detection is based on reflectance at 1.05, 0.88 and 0.66 μm. A cloud shadow algorithm will be developed, otherwise this bit will be replaced with a cloud detection test.

3.2.6 Visible Reflectance Tests

This is a single channel test whose strength is discriminating bright clouds over dark surfaces (e.g., stratus over ocean) and weakness is clouds over bright surfaces (e.g., snow). Two different channels are used in this test dependent on the ecosystem. The 0.66 μm (band 1) is used over oceans, land and polar region. The 0.88 μm reflectance test is also applied over polar and desert scenes. The nominal thresholds are given below.

0.66 μm Reflectance Threshold Test			
Scene Type	Threshold	High confidence clear	Low confidence clear

Day ocean	7.0%	6.5%	8.0%
Day land	16.0%	14.0%	18.0%
Day polar	20.0%	22.0%	18.0%
0.88 μm Reflectance Threshold Test			
Scene Type	Threshold	High confidence	Low confidence
Day polar	10.0%	12.0%	8.0%
Desert	30.0%	26.0%	34.0%

These thresholds are being set based on observations from the AVHRR and MAS. The reflectance test is angular dependent and is also applied in sun glint regions as identified by the sun glint test.

3.2.7 Reflectance Ratio Test

The reflectance ratio test uses channel 19 divided by channel 13 ($r_{.87}/r_{.68}$). This test makes use of the fact that the spectral reflectance at these two wavelengths is similar over clouds (ratio is near 1) and different over water and vegetation. Using AVHRR data this ratio has been found to be between 0.9 and 1.1 in cloudy regions. If the ratio falls within this range, cloud is indicated. New analyses (McClain 1993) suggest that the minimum value may need to be lowered to about 0.8, at least for some cases. For cloud-free ocean the ratio is expected to be less than 0.75 (Saunders and Kriebel 1988). This ratio is generally observed to be greater than 1 over vegetation. Adjustments to the ratio thresholds will be made as necessary for GLI data and must be a function of the ecosystem.

Figure 4 illustrates some of the complexities of desert ecosystems as demonstrated by the visible ratio. The observations are from the AVHRR on the NOAA-9 and are over the Arabian Sea, the Arabian Peninsula, and surrounding regions. The figure shows histograms of ratio values for coastal/water scenes, as well as desert and more densely vegetated areas in the Persian Gulf region from approximately 15-25° N latitude and 50-70° E longitude. Almost all of the observations recorded in the histograms were from clear-sky conditions, as determined by

inspection of visible and IR imagery. As suggested by the histograms of $r_{.87}/r_{.66}$, clear-sky ocean scenes have a ratio of less than 0.75. The surface type classifications are from the Olson World Ecosystems data set. One can immediately see that clear-sky desert values of the visible ratio cover a large range and where that range would indicate cloudy skies for vegetated surfaces. Also note the large amount of overlap between the desert and shrub/grassland categories. This figure shows that clear-sky spectral threshold tests need to be applied very carefully in arid regions and also points out the need for high-resolution ecosystem maps. This test will not be performed over desert, semi-desert and some agricultural ecosystems.

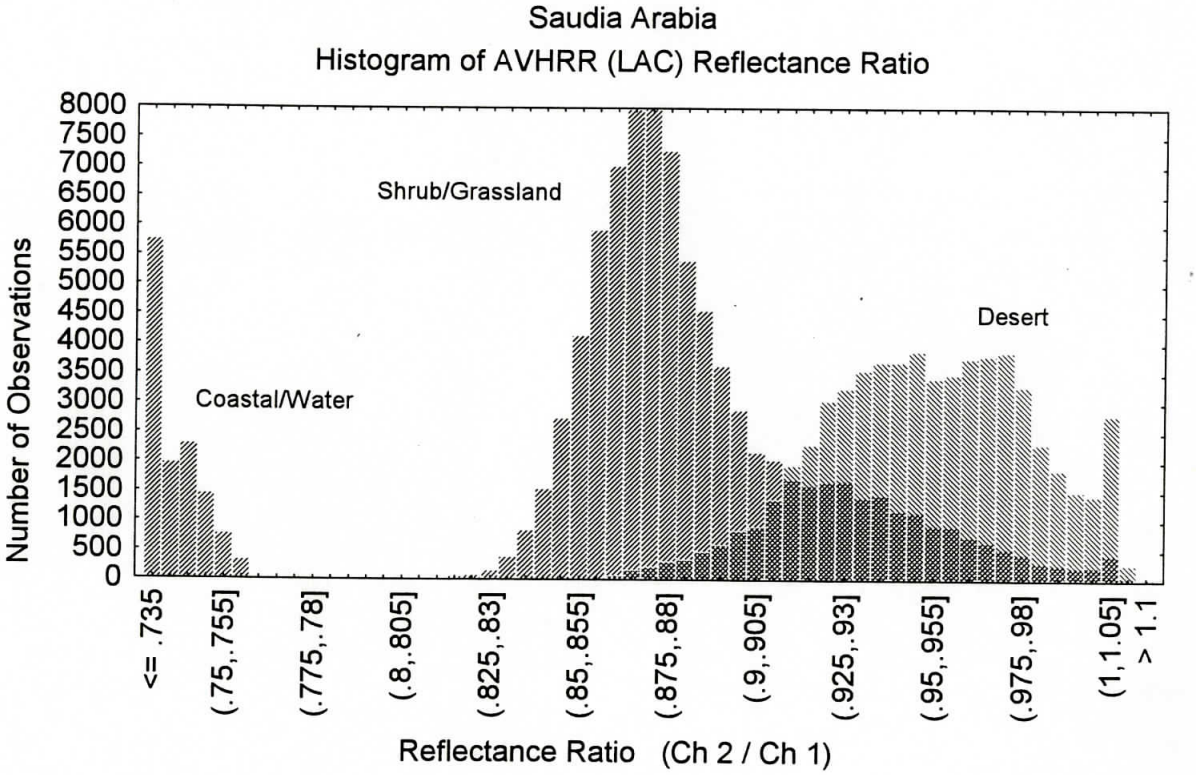

Figure 4. Histogram of the frequency of occurrence of the AVHRR Ch2/Ch1 ratio for a scene over the Arabian peninsula and Arabian Sea.

This ratio test is always performed over water during the day. When applied in regions of possible sun glint, an angular dependency is included in the thresholds. These thresholds are based on analysis of AVHRR LAC and GAC data and the APOLLO algorithm. A histogram analysis of the visible ratio from AVHRR data was performed for 1° increments of reflected sun angle, θ_r (equation 1).

Mixed land and water fields-of-view produce a ratio that is similar to cloud. Thus, coastal regions may be flagged as cloudy.

3.2.8 Confidence Flags

Each of the tests above returns a confidence level ranging from 1 (high confidence that the pixel is clear) to 0 (high confidence that the pixel is cloudy). The individual confidence levels must be combined to determine a final decision on clear or cloudy. We shall denote the confidence level of an individual test as F_i and the final quality flag as Q. There are different methods of combining these individual tests to yield the final quality flag (bits 0 and 1). We have experimented with a variety of methods of combining the confidence of individual tests. The primary effect occurs on the boundaries of the cloud system.

Several tests are not independent of one another. For example, consider daytime over oceans in regions without sun glint. If stratocumulus clouds are present, they will likely be detected by the visible reflectance test, the reflectance ratio test and the BT_{11}-$BT_{3.7}$. These same tests will likely miss the presence of thin uniform cirrus clouds, which would probably be detected by the tri-spectral tests (combinations of BT_8, BT_{11}, and BT_{12}). Very thin cirrus clouds would best be detected by the 1.38 and 13.9 μm micron tests, two tests which have difficulty detecting low level clouds. Because of this overlap in the type of clouds different tests detect, each test is considered in one of four groups. The five groups are:

Group I (Simple IR threshold test)

BT_{11}

$BT_{6.7}$

Group II (Brightness temperature difference)

Tri-spectral test (BT_8 - BT_{11} and BT_{11}- BT_{12})

BT_{11}- $BT_{3.7}$

BT_{11}- $BT_{6.7}$

Group III (Solar reflectance tests)

$r_{0.87}$

$r_{.87}/r_{.66}$

Group IV (NIR thin cirrus)

$r_{1.38}$

Group V (IR thin cirrus)

BT_{11}- BT_{12}

BT_{12}- $BT_{3.7}$

It is likely that the number of these groups will expand in version 2 of the cloud mask. A minimum confidence is determined for each group,

$$G_{i=1,4} = \min[F_i] \tag{15}$$

The final cloud mask is then determined from the product of the results from each group;

$$Q = \sqrt[N]{\prod_{i=1}^{N} G_i} \tag{16}$$

This approach is still clear-sky conservative. If any test is highly confident that the scene is cloudy (F_i=0), the final cloud mask is 00.

The algorithm is divided into eight conceptual domains according to surface type and solar illumination:

1. daytime land surface,
2. daytime water,
3. nighttime land,
4. nighttime water,
5. daytime desert (currently daytime only),
6. nighttime desert (currently daytime only),
7. daytime snow covered regions, and
8. nighttime snow covered regions.

"Daytime" is defined as a solar zenith angle < 85° (and the instrument is in daytime mode). The "desert" classification is based on the 10-minute Olson World Ecosystems data set. A USGS (United States Geological Survey) 1 km land/sea tag file is used for land/water discrimination. For all observations within a given domain, it is generally expected that: 1) the same tests may be performed, and 2) threshold values for each of these tests will not change. Tests defined for nighttime polar or desert observations are still under development. The default nighttime land

algorithm is substituted in both cases. It is expected that more domains will be established in the future.

3.2.9 Radiance Spatial Uniformity

The infrared window spatial uniformity test (applied on 3 by 3 pixel segments) is effective over water and is to be used with caution in other situations. Most ocean regions are well suited for spatial uniformity tests; such tests may be applied with less confidence in coastal regions or regions with large temperature gradients (e.g., the Gulf Stream). Various spatial tests exist such as the spatial coherence and the ISCCP space contrast test.

The spatial coherence test (Coakley and Bretherton, 1982) is based on the assumption of a uniform background and single-layered, optically thick cloud systems. The method is based upon the computation of the mean and standard deviation for a group of pixels using 11 μm radiances. When the standard deviation is plotted versus the mean, an arch shaped structure is often observed. The warm pixels with low values of standard deviation are assumed to be clear regions. The clear-sky FOVs can be selected as those within a standard deviation threshold (which is fixed at a small value) of the warm foot of the arch. Note that the derived clear-sky foot of the arch should have a temperature consistent with the thresholds derived using the individual FOV tests.

The ISSCP space contrast (sc) test, described in Rossow and Garder (1993), is similar to that of spatial coherence and is physically based upon the fact that clear pixels tend to be warmer than cloudy pixels and exhibit less spatial variability. First, for a small local region the pixel with the largest brightness temperature (BT_{11}^{max}) is found. All pixels colder than the spatial contrast ($BT_{11}^{max} - \Delta_{sc}$) value are labeled as cloudy; all others, including the warmest pixel are labeled as undecided. The size of the contrast threshold must be larger than the magnitude of natural variation at the surface and smaller than that caused by clouds. Values of Δ_{sc} near 3.5°C are common over ocean regions. It is important that the class of pixels be identical and that the size of the region be chosen carefully. When extending into coastal regions and land regions containing mixed land and water, pixels are excluded from this test since the inherent contrast between land and water surface radiances would dominate the results. For regions that are too large, there is increased likelihood of spatial variations in surface parameters. The shape of the test regions can

also be important since meridional gradients in surface temperature generally are larger than zonal gradients.

Similar spatial tests will be incorporated into the GLI cloud mask for uncertain obstructed FOVs. The specific test will likely depend on how the data stream is structured regarding the ease of compositing pixels over geographic regions. Uniform stratus can also give the appearance of a uniform ocean, thus the spatial tests must often complement the threshold tests (e.g., the tri-spectral test).

The GLI cloud mask currently uses a spatial variability test over oceans and large lakes. The tests are used to modify the confidence of a pixel being clear. If the confidence flag of a pixel is < 0.95, the variability test is implemented. If the difference between the pixel of interest and any of the surrounding pixel brightness temperatures is $>0.5°C$, the scene is considered variable and the confidence lowered.

Surface temperature variability, both spatial and temporal, is larger over land than ocean, making land scene spatial uniformity tests difficult. GLI spatial uniformity tests over land will be constrained to similar ecosystems in a given geographic regime. These tests have yet to be developed.

The reflectance uniformity test (similar to CLAVR) is applied by computing the maximum and minimum values of GLI 0.66 μm or 0.87 μm reflectances within a 3 x 3 pixel array. Pixel arrays with band 1 reflectance differences greater than threshold 1 (around 9%) over land or band 2 reflectance differences greater than threshold 2 (possibly 0.3%) over ocean are labeled in CLAVR as mixed (Stowe et al. 1993). The value over ocean is low because a cloud-free ocean is almost uniformly reflective, while non-uniformity is assumed to be caused by cloudiness. This test will be refined for GLI applications.

3.2.10 Clear-Sky Radiance Composite Maps

Composite maps have been found to be very useful by ISSCP. The MODIS cloud mask relies on composite maps, but to a lesser extent than ISCCP since the advantages of higher spatial resolution and more spectral bands will change the application and the need. The disadvantage of composite maps is the large memory and CPU required for effective application. To reduce

storage and CPU requirements, we are not planning on making use of clear-sky radiance composite maps for the GLI cloud mask algorithm.

4.0 Practical Application of Cloud Detection Algorithms

To review:

The algorithm is divided into eight conceptual domains according to surface type and solar illumination: daytime land surface, daytime water, nighttime land, nighttime water, daytime desert, nighttime desert, and daytime and nighttime polar regions. "Daytime" is defined as a solar zenith angle < 85° while "polar" currently refers to any region poleward of 60° latitude. The "desert" classification is based on the 10-minute Olson World Ecosystems data set. A USGS (United States Geological Survey) 1 km land/sea tag file is used for land/water discrimination. For all observations within a given domain, it is generally expected that: 1) the same tests may be performed, and 2) threshold values for each of these tests will not change. As yet, there are no sets of tests defined for nighttime polar or desert observations. The default nighttime land algorithm is substituted in both cases. It is expected that more domains will be established in the future.

Once a pixel has been assigned to a particular domain, the spectral data corresponding to that location are subjected to a series of threshold tests designed to detect the presence of clouds in the instrument FOV. These tests are the heart of the cloud mask algorithm. There are several types of tests, none of which are equally good at detecting all cloud conditions. For example, some are more reliable for low cloud or thin cirrus cloud detection, while others are better at finding any kind of optically thick cloud. Accordingly, tests which indicate similar cloud conditions are grouped together to obtain several intermediate results that are then combined to form a final cloud mask value. The tests are grouped so that independence between them is maximized. All tests which detect thin cirrus might make up a group, for example, while those which find high, cold clouds would form another, and low-level cloud detection tests could make a third set. Of course, few if any spectral tests are completely independent of all the others.

The result of each spectral threshold test is expressed as a "confidence" which indicates the strength of the observed radiance signature compared to that which is expected for the cloud condition in question. For example, one very fundamental test performed for water surfaces is the "cold cloud test." Over open waters any scene with an observed 11 μm brightness temperature

colder than ~270°K must be at least partially cloudy. Therefore, the threshold value for this test is set at that value. The actual cutoff temperature for any given FOV varies slightly, however, because of differing amounts of atmospheric water vapor attenuation due to changes in actual water vapor content or instrument viewing angle. Consequently, a "confidence window" is constructed with boundaries at 267° and 273°K. Since the ultimate goal of the algorithm is to specify a confidence of clear-sky, an observed brightness temperature of < 267°K is defined to have 0 confidence while a measurement of > 273°K has 1.00 confidence. *Note that this confidence does not yet refer to clear-sky conditions, only to the particular condition tested for.* In this case it indicates only the extent of confidence that the FOV did *not* contain significant amounts of opaque, cold clouds. Observations between 267° and 273°K result in confidences ranging linearly between 0 and 100%. Figure 3 showed an example of the relationship between test thresholds and confidence boundaries. Note that the threshold value corresponds to a confidence of 50%.

When all tests within a group have been performed, the minimum resulting confidence from among them is taken to be representative of that group. Then the other groups of tests are performed with group confidences determined in the same way. These confidences indicate absence of particular cloud types. A final step is to combine the group confidences, assumed to be independent, by multiplying them together. Only at this point does the confidence value reflect the surety of clear-sky conditions.

Using this algorithm, most observations have either high confidences (> 0.95) or very low confidences (< 0.05) of unobstructed views of the surface. There are always those difficult scenes, however, which result in intermediate values of the cloud mask. These tend to be found at cloud boundaries, or where low clouds are found over water surfaces at night, or over certain land surfaces such as desert or other sparsely-vegetated regions. In these cases (final confidence > 0.05 and <0.95), spatial and/or temporal continuity tests are conducted. Currently, only spatial continuity testing has been implemented and this only for water surfaces. 11 μm brightness temperature differences between the pixel of interest and the surrounding eight are checked for consistency. If all the differences are less than 0.5 K, the confidence is adjusted upward by one "level" (e.g. > 0.66 to > 0.95).

4.1 Ancillary Data Set Requirements

A number of preprocessing steps will be made before the cloud masking algorithm is applied. First, each pixel in the scene will be tagged as being land or water, and if land, a land/water percentage. Second, each land pixel will be classified as to its ecosystem and its elevation will be designated as relatively flat, valley, isolated mountainous region, low mountains or hills, generally mountainous, or extremely rugged mountains.

Information on surface temperature and sea state will be sought from surface observations, Reynolds blended analysis, and NMC model 3-hour surface analyses of temperature.

4.2 Implementation of the Cloud Mask Algorithms

4.2.1 Outline of cloud mask algorithm

The hierarchical approach used in version 1 of the cloud mask is:

(1) Determine if the pixel is of a land or water scene.

(2) Determine the ecosystem type.

(3) Determine if pixel is in a sun glint region.

(4) Determine if the pixel is in a day or night regime.

(5) Retrieve information from snow cover and ice data base.

(6) Apply appropriate single FOV masking tests and set initial unobstructed FOV determination for the given domain. Initial confidence flag is assigned for each test result, depending on its relative position to the threshold (see Section 3).

- For daytime testing, solar zenith angles are constrained to be less than 85°.
- Ocean tests are applied to open ocean and for large lakes.
- Sun glint occurs when the reflected sun angle lies between 0° and 36°.
- The land algorithm is applied to non-desert and non-water areas.
- The desert algorithm is applied to desert ecosystems.
- The snow algorithm is applied to regions passing the NSDI test.

- For the single pixel clear-sky determination, 11 single FOV tests are implemented and an obstructed/not obstructed bit set (0 for obstructed, 1 for clear) for each test.

(7) The single FOV cloud test results are grouped and the minimum of each group determined.

(8) The group minimums are then multiplied together, and the N^{th} root taken (where N represents the number of groups) producing the initial cloud mask (Section 3.2.8). If any of the individual tests are high confidence cloudy (clear confidence of 0), the product is zero.

(9) If confidence level is still uncertain (between 0.05 and < 0.95), use spatial uniformity tests on 3×3 pixel regions (Currently not implemented over land).

- Spatial IR variability test applied with band 31 using $\Delta_{SV} = 0.50$ K over water.
- Adjust quality flag if appropriate by increasing or decreasing confidence levels.

(10) Output cloud mask.

4.2.2 Cloud mask examples

The cloud mask algorithm has been applied to several data sets selected by the cloud mask group, as well as scenes selected by other science team members. This section includes several examples of the output from the current version of the GLI cloud mask. It is not intended as a validation section, but rather as a visual indication of the success and problems of the current version.

AVHRR cloud mask Data sets

Figure 5 is a three panel image of NOAA-14 AVHRR GAC observations. The left most panel is the channel 1 (0.6 μm) image and the middle panel the channel 4 (11 μm) image. The scene is over the tropical Pacific Ocean. The resulting cloud mask output file is represented in the right most panel. The legend is as follows

Black: High confident clear (bits 1-2 equal 11)

Dark Gray: Probably clear (bits 1-2 equal 10)

Light Gray: Maybe Clear(bits 1-2 equal 01)

White: High confident obstructed FOV (bits 1-2 equal 00)

Notice that the confidence in clear-sky scene tends to drop over the sun glint region, as it is difficult to detect clouds in areas affected by sun glint. The additional channels of GLI should improve our clear-sky detection capabilities in sun glint regions.

Another 3 panel image of NOAA-14 AVHRR GAC observations is shown in Figure 6. This scene includes parts of North Africa and the Atlantic Ocean. The *blocky* structure of the cloud mask over land results from the 10-minute ecosystem map; land spectral tests are being applied to desert regions. This points to the need for an accurate global 1 km ecosystem map, one that is consistent with the land/sea map. The high confidence obstructed scenes over the Saharan region is a dust storm. Most of this dust storm has negative values of BT_{11}-BT_{12}, setting the aerosol obstruction bit to zero (bit 8 in the mask output file).

Future AVHRR Data Processing

An entire month of AVHRR GAC data has been obtained from the AVHRR Pathfinder Program. This data set is being processed to gain further experience with implementing clear-sky

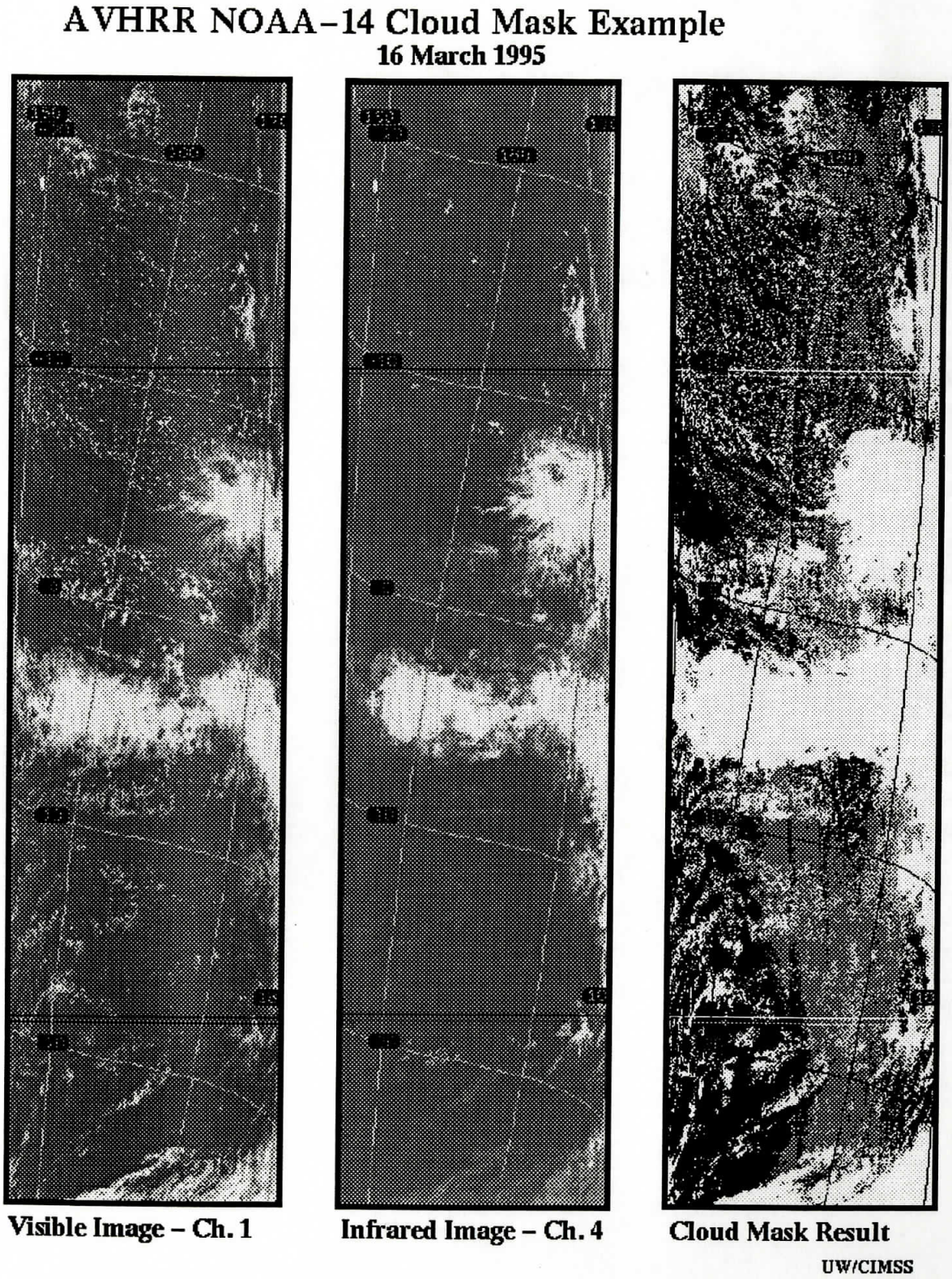

Figure 5. An example of the cloud mask derived from AVHRR data for a scene over the Pacific Ocean (right hand panel), together with images from two of the AVHRR bands used in generating the mask.

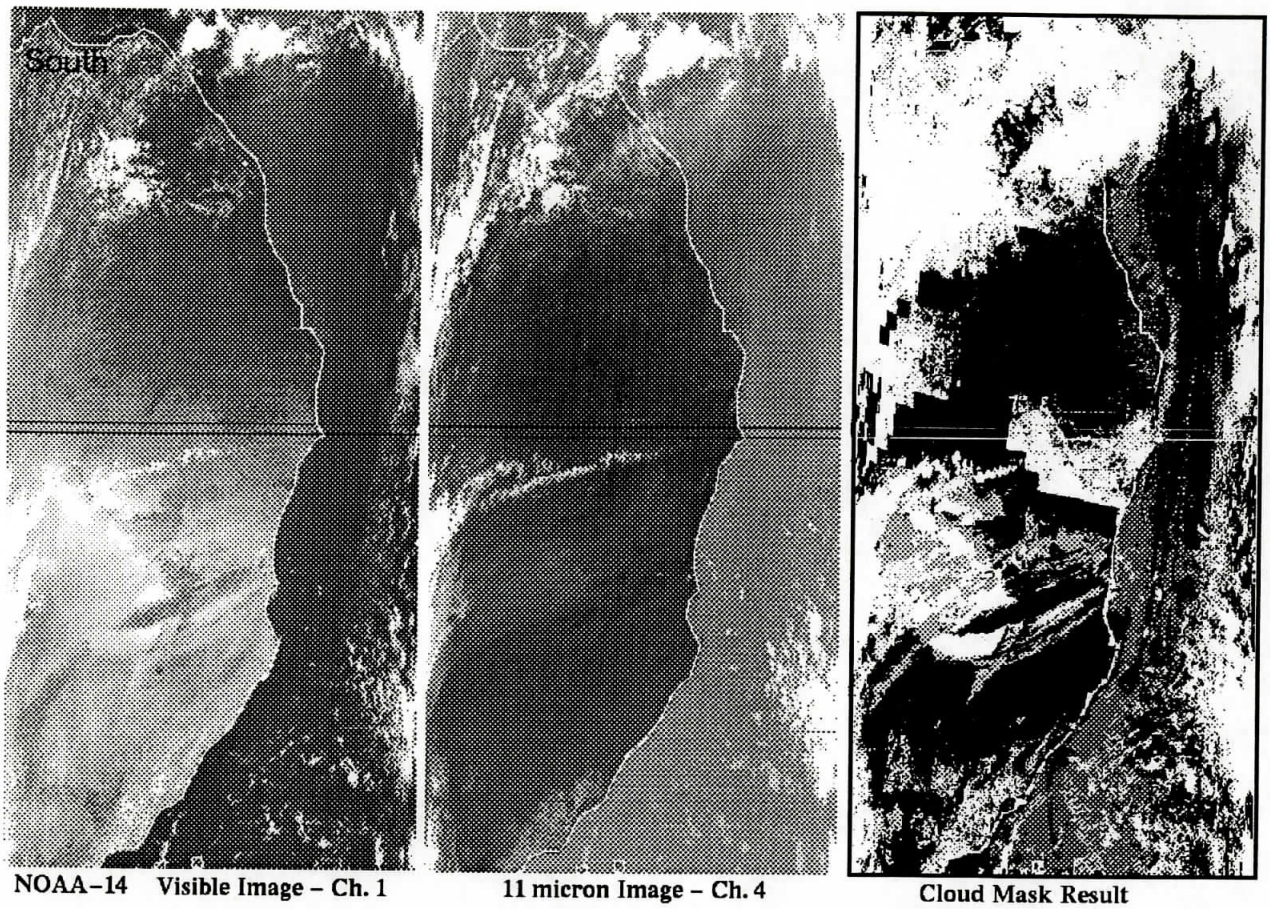

Figure 6. An example cloud mask, together with images at two AVHRR bands, obtained over the eastern Atlantic and west Africa. South is at the top of the figure.

MAS cloud mask data sets

The cloud masking algorithm has also been applied to several MAS scenes. Here we present results from two scenes of the MAS 50 channel data set. The first scene is from observations made on 7 June 1995 over the north slope of Alaska (tundra). The MAS has a spatial resolution of approximate 50 m. Figure 7 includes the visible, infrared, and the final cloud mask. Results from individual tests are available from the authors.

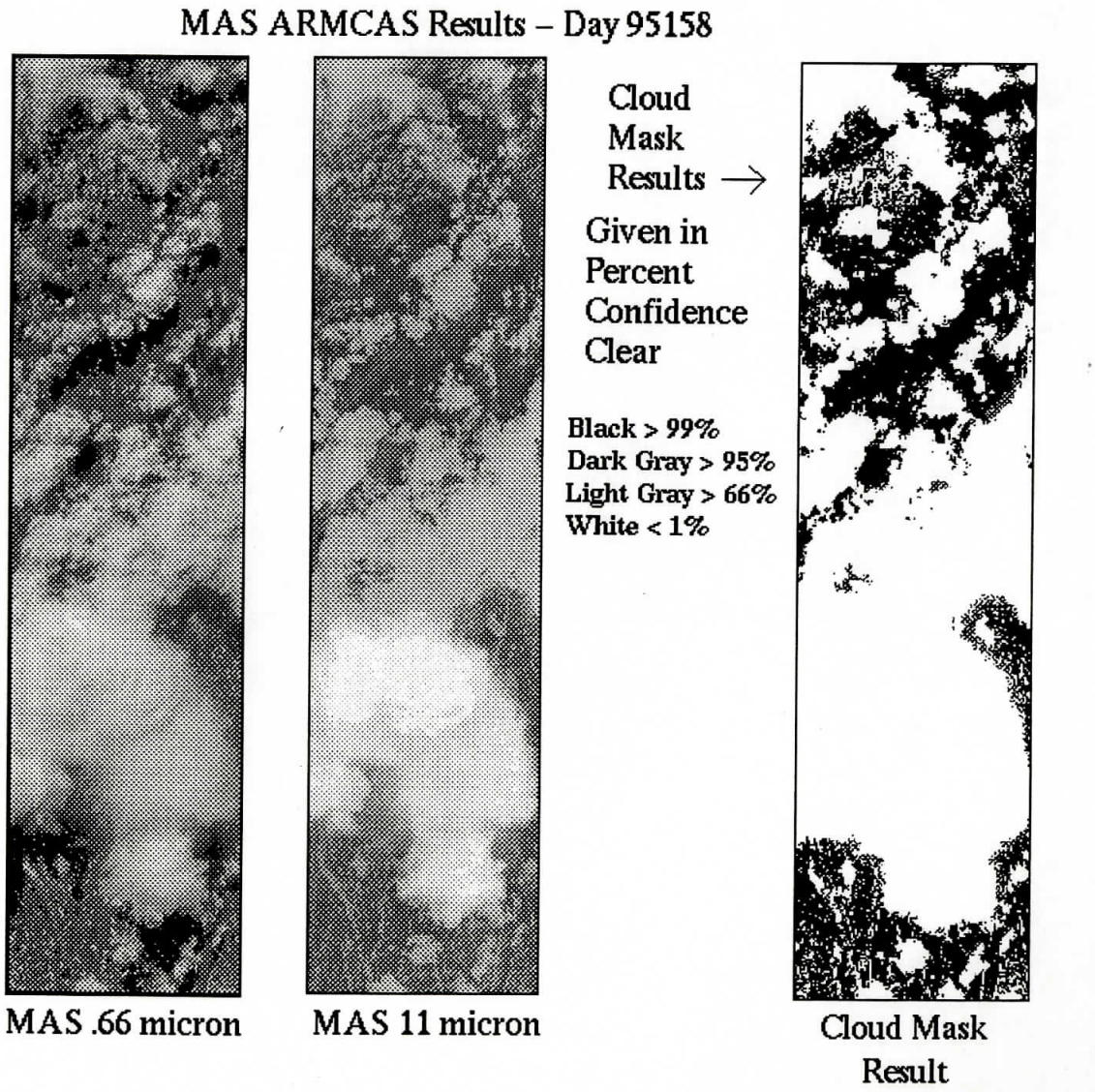

Figure 7. An example cloud mask output using MAS data obtained over the north slope of Alaska on 7 June 1995.

The second example of an application of the MAS cloud mask (Figure 8) is of a scene from ARMCAS provided by Dr. S. -C. Tsay. This scene is cloud free, but includes both dark tundra and light sea ice, thus all pixels indicated as high confident cloudy are false detections. Many of these falsely detected scenes result from failing the 1.88 μm test. Causes and solutions for these failures are under investigation.

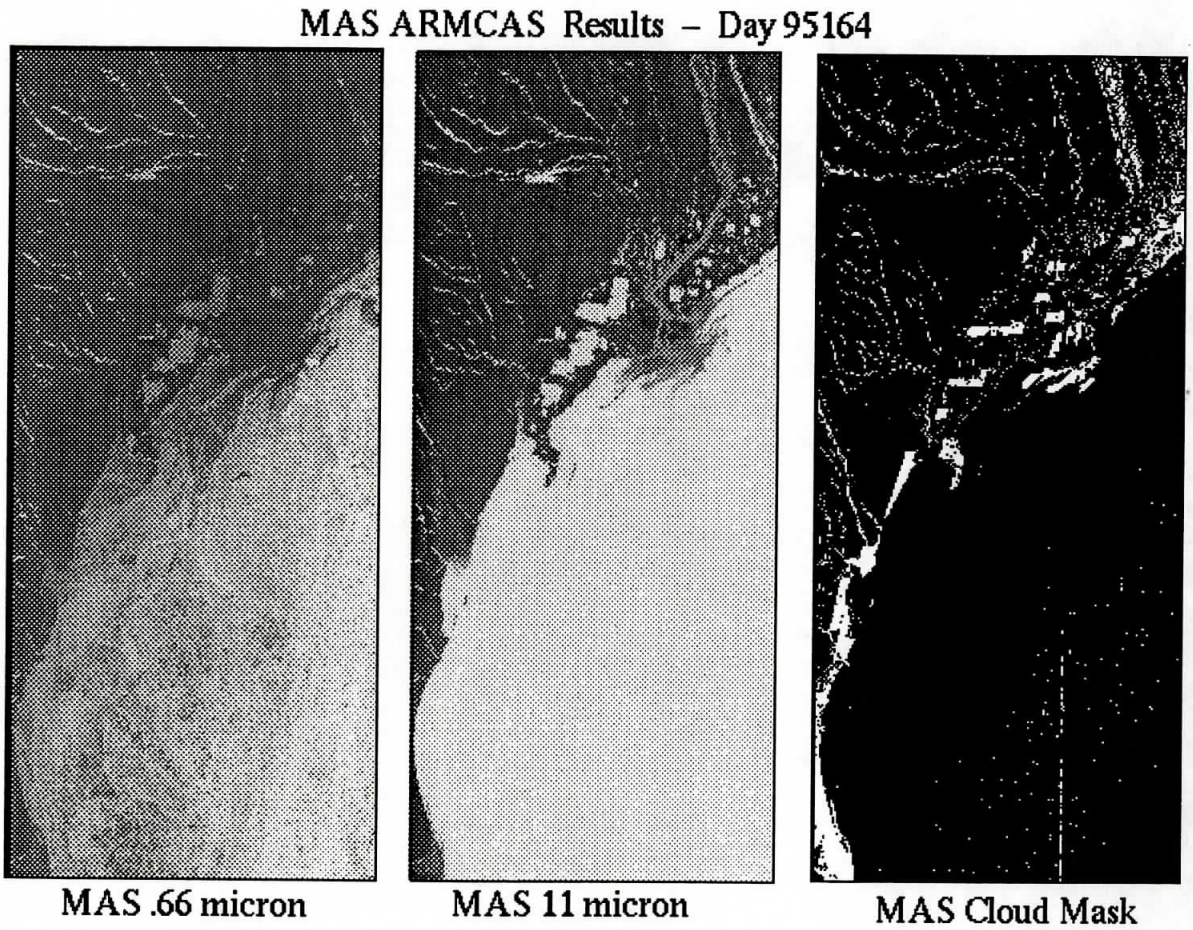

Figure 8. An example cloud mask output using MAS data obtained near Prudhoe Bay and sea ice in the Beaufort Sea on 13 June 1996.

Future MAS Data Processing

The University of Wisconsin-Madison will be applying and validating the MAS cloud mask using data from the recent SUCCESS experiment. The code is available for other GLI team members. The MAS cloud mask code which simulates the GLI cloud mask, and reads the

Goddard MAS HDF data format, will be available to all GLI science team members in August 1997.

4.3 Numerical Programming Considerations

A version of the GLI mask currently operates on MAS data is available for testing. Based on comparison with MODIS cloud mask processing, we estimate the GLI cloud mask to require an output volume load 1.5 GB/day. The product volume is expected to be slightly greater than this with the addition of metadata fields.

4.4 Development Plan

The GLI cloud mask algorithms build on existing programs, particularly the MODIS program; however, much work yet remains to develop and implement the algorithms by launch. Some of the approaches outlined in the document can be developed with current satellite observations, while others require modeling efforts and regional observations with the MODIS Airborne Simulator (MAS).

Our research and development strategy makes use of three data sets. The first is a global data set of collocated HIRS/2 and AVHRR GAC (Global Area Coverage) observations. The strengths of this data set are its global coverage and that the collocated observations have many GLI like bandwidths. This allows us to investigate many of the spectral tests described above. The disadvantage of the data set is the large FOV (HIRS/2 FOV is 17 km at nadir) and the horizontal displacement of the HIRS/2 footprints (gaps of approximately 20 km). This data set also does not have the complete AVHRR image, only those AVHRR pixels that lie within the HIRS/2 footprint. To overcome this later disadvantage we have compiled a second data set of collocated HIRS/2 and AVHRR LAC (Local Area Coverage) observations. This data set has similar spectral and spatial resolution to the future GLI and will be important for validation and development of cloud shadow detection techniques. The disadvantages, of course, are the non-global nature and the gaps between the HIRS FOV.

The third data set is from the MAS aircraft flights. The initial MAS instrument recorded twelve (or eleven) spectral bands in the visible to infrared and enabled development and exploration of some of the techniques discussed above. Since December 1994, the MAS recorded 50 spectral channels, this data will play an important role in testing and developing the mask.

We recognize the need to work closely with the GLI land, ocean, and atmosphere groups in the continued development of the cloud mask. To this end we have offered to process different MAS and AVHRR data scenes for examination. We have developed the FORTRAN code to read the Goddard HDF MAS 50 channel data format and output a cloud mask similar in structure to the GLI 16 bit cloud mask. *This code is available to GLI science team members to test the cloud mask and assist in its development.*

4.5 Validation Plan

Validation will be approached in several ways: (i) collocation with higher resolution aircraft data, (ii) ground-based observations, and (iii) intercomparisons with other AM-1 platform instruments. Our validation approach relies heavily on the sources of data used in the algorithm development, which consisted primarily of the MAS, a fifty channel visible, near-infrared, and thermal infrared imaging spectrometer with 50 m resolution at nadir (King et al. 1996); HIS, a 2 km resolution nadir-viewing Michelson interferometer with 0.5 cm^{-1} spectral resolution from 4 to 15 μm (Revercomb et al. 1988); and AVIRIS, a 224 band imaging spectrometer from 0.4-2.5 μm with 20 m resolution at nadir (Vane et al. 1993). In addition, we plan to make extensive use of the AERONET (Aerosol Robotic Network), a network of ground-based sunphotometers established and maintained by Brent Holben that measure the spectral aerosol optical thickness and sky radiance, reporting the data via a satellite communication link from each remotely-located CIMEL sunphotometer to Goddard Space Flight Center from sunrise to sunset, 7 days a week. Finally, we plan to utilize ground-based radar, lidar, and radiometer observations, especially over the Atmospheric Radiation Measurement (ARM) CART (Clouds And Radiation Testbed) site in Oklahoma.

Comparison of GLI radiances and products with those from other instruments should be made periodically (perhaps annually) in different seasons in daytime and nighttime conditions. We

anticipate numerous opportunities, unspecified, in which scientists worldwide will compare GLI-derived atmospheric, land, and ocean data products with local measurements of the geophysical property of interest. This wide-scale synthesis of data sets obtained from scientists of Australia, Japan, China, Europe, South America, and Africa will greatly enhance the confidence that we place in the GLI-derived products, and will, with time, aid our ability to assess the quality of the data products from a wide variety of climatic conditions and seasons.

5.0 References

Ackerman, S. A., W. L. Smith and H. E. Revercomb, 1990: The 27-28 October 1986 FIRE IFO cirrus case study: Spectral properties of cirrus clouds in the 8-12 micron window. *Mon. Wea. Rev.*, **118**, 2377-2388.

Allen, R. C., Jr., P. A. Durkee and C. H. Wash, 1990: Snow/cloud discrimination with multispectral satellite measurements. *J. Appl. Meteor.*, **29**, 994-1004.

Arking, A., and J. D. Childs, 1985: Retrieval of cloud cover parameters from multispectral satellite images. *J. Climate Appl. Meteor.*, **24**, 322-333.

Baum, B. A., T. Uttal, M. Poellot, T. P. Ackerman, J. M. Alvarez, J. Intrieri, D. O'C. Starr, J. Titlow, V. Tovinkere, and E. Clothiaux, 1995: Satellite remote sensing of multiple cloud layers. *J. Atmos. Sci.*, **52**, 4210-4230.

Baum, B. A., B. A. Wielicki, and P. Minnis, 1992: Cloud-property retrieval using merged HIRS and AVHRR data. *J. Appl. Meteor.*, **31**, 351-369.

Ben-Dor, E., 1994: A precaution regarding cirrus cloud detection from airborne imaging spectrometer data using the 1.38 micron water vapor band. *Remote Sens. Environ.*, **50**, 346-350.

Berendes, T., S. K. Sengupta, R. M. Welch, B. A. Wielicki, and M. Navar, 1992: Cumulus cloud base height estimation from high spatial resolution data: A Hough transform approach. *IEEE Trans. Geosci. Remote Sens.*, **30**, 430-443.

Booth, A. L., 1973: Objective cloud type classification using visual and infrared satellite data. 3rd Conference on Probability and Statistics in the Atmospheric Sciences. Amer. Meteor. Soc., Boulder, CO.

Brooks, D. R., E. F. Harrison, P. Minnis, J. T. Suttles, and R. S. Kandel, 1986: Development of algorithms for understanding the temporal variability of the earth's radiation balance. *Rev. Geophys.*, **24**, 422-438.

Chen, D. W., S. K. Sengupta, and R. M. Welch, 1989: Cloud field classification based upon high spatial resolution textural features, Part 2, Simplified vector approaches, *J. Geophys. Res.*, **94**, 14749-14765.

Coakley, J. A, 1987: A dynamic threshold method for obtaining cloud cover from satellite imagery data. *J. Geophys. Res.*, **92**, 3985-3990.

Coakley, J. A. and F. P. Bretherton, 1982: Cloud cover from high-resolution scanner data: Detecting and allowing for partially filled fields of view. *J. Geophys. Res.*, **87**, 4917-4932.

Derrien, M., B. Fraki, L. Harang, H. Legleau, A. Noyalet, D. Pochic, and A. Sairouni, 1993: Automatic cloud detection applied to NOAA-11 AVHRR imagery. *Remote Sens. Environ.*, **46**, 246-267.

Deschamps, P. Y. and T. Phulpin, 1979: Atmospheric correction of infrared measurements of sea surface temperature using channels at 3.7, 11, and 12 microns. *Boundary Layer Meteor.*, **18**, 131-143.

Ebert, E. E., 1987: A pattern-recognition technique for distinguishing surface and cloud types in the polar-regions. *J. Climate Appl. Meteor.*, **26**, 1412-1427.

Ebert, E., 1989: Analysis of polar clouds from satellite imagery using pattern recognition and a statistical cloud analysis scheme. *J. Appl. Meteor.*, **28**, 382-399.

Franca, G. B., and A. P. Cracknell, 1995: A simple cloud masking approach using NOAA AVHRR daytime data for tropical areas. *Int. J. Remote Sens.*, **16**, 1697-1705.

Francis, Jennifer A., 1994: Improvements to TOVS retrievals over sea ice and applications to estimating Arctic energy fluxes. *J. Geophys. Res.*, **99**, 10395-10408.

Gao, B.-C., A. F. H. Goetz, and W. J. Wiscombe, 1993: Cirrus cloud detection from airborne imaging spectrometer data using the 1.38 micron water vapor band. *Geophys. Res. Lett.*, **20**, 301-304.

Gao, B.-C., and A. F. H. Goetz, 1991: Cloud area determination from AVIRIS data using water vapor channels near 1 micron. *J. Geophys. Res.*, **96**, 2857-2864.

Garand, L., 1988: Automated recognition of oceanic cloud patterns. Part I: Methodology and application to cloud climatology. *J. Climate*, **1**, 20-39.

Giarratano, J. and G. Riley, 1989: Expert systems: Principles and programming, PWS-KENT Publishing Company, Boston, 632pp.

Gustafson, Gary B., Ronald G. Isaacs, Robert P. d'Entremont, Jeanne M. Sparrow, Thomas M. Hamill, Christopher Grassotti, Douglas W. Johnson, Charles P. Sarkisian, Daniel C. Peduzzi, Brian T. Pearson, Vida D. Jakabhazy, James S. Belfiore, Anthony S. Lisa, 1994: Support of environmental requirements for cloud analysis and archive (SERCAA): Algorithm descriptions. Scientific Report No. 2, 28 March 1994. Phillips Laboratory, Directorate of Geophysics, Air Force Material Command, Hanscom Air Force Base, MA.

Gutman, G., D. Tarpley, and G. Ohring, 1987: Cloud screening for determination of land surface characterisitics in a reduced resolution satellite data set. *Int. J. Remote Sens.*, **8**, 859-870.

Hall, D.K., Riggs, G.A. and Salomonson, V.V. 1995: Development of methods for mapping global snow cover using Moderate Resolution Imaging Spectroradiometer data, *Remote Sens. Env.*, **54,**127-140.

Haralick, R. M., K. S. Shammugam, and I. Dinstein, 1973: Textural features for image classification. *IEEE Trans. On Systems, Man, and Cybernetics*, Vol. **SMC-3**, No. 6, 610-621.

Hayden, C. M., G. S. Wade, and T. J. Schmit, 1996: Derived product imagery from GOES-8. *J. Appl. Meteor.*, **35**, 153-162.

Hecht-Nielsen, R., 1990: Neurocomputing. Addison-Wesley, Reading, MA, 430 pp.

Hou, Y-T., K. A. Campana, K. E. Mitchell, S. K. Lang, and L. L. Stowe, 1993: Comparison of an experimental NOAA AVHRR cloud dataset with other observed and forecast cloud datasets. *J. Atmos. Oceanic Technol.*, **10**, 833-848.

Hunt, G. E., 1973: Radiative properties of terrestrial clouds at visible and infrared thermal window wavelengths. *Quart. J. Roy. Meteor. Soc.*, **99**, 346-369.

Hutchison, K. D., and K. R. Hardy, 1995: Threshold functions for automated cloud analyses of global meteorological satelitte imagery. *Int. J. Remote Sens.*, **16**, 3665-3680.

Inoue, T., 1986: On the temperature and effective emissivity determination of semi-transparent clouds by bi-spectral measurements in the 10 micron window region. *J. Meteor. Soc. Japan*, **63**, 88-99.

Inoue, T., 1987: A cloud type classification with NOAA 7 split window measurements. *J. Geophys. Res.*, **92**, 3991-4000.

Inoue, T., 1989: Features of clouds over the Tropical Pacific during the Northern Hemispheric winter derived from split window measurements. *J. Meteor. Soc. Japan*, **67**, 621-637.

Jacobowitz, H. J., 1970: Emission scattering and absorption of radiation in cirrus clouds. Ph.D. thesis, Massachusetts Institute of Technology, 181 pp.

Kaufman, Y. J., 1987: Satellite sensing of aerosol absorption. *J. Geophys. Res.*, **92**, 4307-4317.

Kaufman, Y. J., and C. Sendra, 1988: Algorithm for atmospheric corrections of visible and near IR satellite imagery. *Int. J. Remote Sens.*, **9**, 1357-1381.

Kaufman, Y. J., and T. Nakajima, 1993: Effect of Amazon smoke on cloud microphysics and albedo - analysis from satellite imagery. *J. Appl. Meteo.*, **32**, 729-744.

Key, J. and R. G. Barry, 1989: Cloud cover analysis with Arctic AVHRR data. 1. Cloud detection. *J. Geophys. Res.*, **94**, 8521-8535.

King, M. D., Y. J. Kaufman, W. P. Menzel and D. Tanré, 1992: Remote sensing of cloud, aerosol, and water vapor properties from the Moderate Resolution Imaging Spectrometer (MODIS). *IEEE Trans. Geosci. Remote Sens.*, **30**, 2–27.

King, M. D., W. P. Menzel, P. S. Grant, J. S. Myers, G. T. Arnold, S. E. Platnick, L. E. Gumley, S. C. Tsay, C. C. Moeller, M. Fitzgerald, K. S. Brown and F. G. Osterwisch, 1996: Airborne scanning spectrometer for remote sensing of cloud, aerosol, water vapor and surface properties. *J. Atmos. Oceanic Technol.*, **13**, 777–794.

King, Michael D., Lawrence F. Radke, and Peter V. Hobbs, 1993: Optical properties of marine stratocumulus couds modified by ships. *J. Geophys. Res.*, **98**, 2729-2739.

Kriebel, K. T., 1978: Measured spectral bidirectional reflection properties of four vegetated surfaces. *Appl. Opt.*, **17**, 253-259.

Lee, J., R. Weger, S. K. Sengupta, and R. M. Welch, 1990: A neural network approach to cloud classification. *IEEE Trans. Geosci. and Remote Sens.*, **28**, 846-855.

Lindsay, R. W. and D. A. Rothrock, 1994: Arctic sea ice surface temperature from AVHRR. *J. Climate*, 7, 174-183.

Liou, K. N., 1973: A numerical experiment on Chandrasekhar's discrete-ordinate method for radiative transfer: Applications to cloudy and hazy atmospheres. *J. Atmos. Sci.*, **30**, 1303-1326.

Liou, K. N., S. C. Ou, Y. Takano, F. P. J. Valero, and T. P. Ackerman, 1990: Remote sounding of the tropical cirrus cloud temperature and optical depth using 6.5 and 10.5 μm Radiometers during STEP. *J. Appl. Meteor.*, **29**, 716-726.

Luger, G. F. and W. A. Stubblefield, 1989: Artificial intelligence and the design of expert systems, The Benjamin Cummings Publishing Company, Inc., 600 pp.

Matthews, E. and W. B. Rossow, 1987: Regional and seasonal variations of surface reflectance from satellite observations at 0.6 mm. *J. Climate Appl. Meteor.*, **26**, 170-202.

McClain, E. P., 1993: Evaluation of CLAVR Phase-I algorithm performance: Final Report, U. S. Department of Commerce/NOAA/NESDIS, Report 40-AANE-201-424.

McMillin, L. M., and C. Dean, 1982: Evaluation of a new operational technique for porducing clear radainces. *J. Appl. Meteor.*, **12**, 1005-1014.

McMillin, Larry, Si-Song Zhou, and Shi-Keng Yang, 1994: An improved cloud retrieval algorithm using HIRS2-MSU radiance measurements. *J. Appl. Meteor.*, **33**, 195-211.

Meerkoetter, R., 1993: Detection of polar stratospheric clouds with next generation IR sounders. NATO ASI Series, 19, 205-213.

Menzel, W. P. and K. I. Strabala, 1989: Preliminary report on the demonstration of the VAS CO_2 cloud parameters (cover, height, and amount) in support of the Automated Surface Observing System (ASOS). NOAA Tech Memo NESDIS 29.

Menzel, W. P., D. P. Wylie, and K. I. Strabala, 1992: Seasonal and diurnal changes in cirrus clouds as seen in four years of observations with the VAS. *J. Appl. Meteor.*, **31**, 370-385.

Menzel, W. P., D. P. Wylie, and K. I. Strabala, 1993: Trends in global cirrus inferred from four years of HIRS data. Technical Proceedings of the Seventh International TOVS Study Conference held 10-16 February in Igls, Austria.

Minnis, P. and E. F. Harrison, 1984a: Diurnal variability of regional cloud and clear sky radiative parameters derived from GOES data. Part I: Analysis method. *J. Climate Appl. Meteor.*, **23**, 993-1011.

Minnis, P. and E. F. Harrison, 1984b: Diurnal variability of regional cloud and clear sky radiative parameters derived from GOES data. Part II: November 1978 cloud distributions. *J. Climate Appl. Meteor.*, **23**, 1012-1031.

Minnis, P., and E. F. Harrison, 1984c: Diurnal variability of regional cloud and clear-sky radiative parameters derived from GOES data, Part III: November 1978 radiative parameters. *J. Climate Appl. Meteor.*, **23**, 1032-1051.

Minnis, P., E. F. Harrison and G. G. Gibson, 1987: Cloud cover over the eastern equatorial Pacific derived from July 1983 ISCCP data using a hybrid bispectral threshold method. *J. Geophys. Res.*, **92**, 4051-4073.

Minnis, P., W. L. Smith, Jr., D. P. Garber, J. K. Ayers, and D. R. Doelling, 1995: Cloud Properties Derived From GOES-7 for Spring 1994 ARM Intensive Observing Period Using Version 1.0.0 of ARM Satellite Data Analysis Program. NASA Reference Publication 1366.

Mokhov, I. I. and M. E. Schlesinger, 1994: Analysis of global cloudiness. 2. Comparison of ground-based and satellite-based cloud climatologies. *J. Geophy. Res.*, **99**, 17045-17065.

Molnar, G. and J. A. Coakley, Jr., 1985: Retrieval of cloud cover from satellite imagery data: a statistical approach. *J. Geophy. Res.*, **90**, 12960-12970.

O'Brien, D. M., and R. M. Mitchell, 1992: Error estimates for retrieval of cloud-top pressure using absorption in the A band of oxygen. *J. Appl. Meteor.*, **31**,1179-1192.

Ou, S. C., K. N. Liou, W. M. Gooch, and Y. Takano, 1993: Remote sensing of cirrus cloud parameters using advanced very-high-resolution radiometer 3.7- and 10.9-um channels. *Appl. Opt.*, **32**, No. 12, 2171-2180.

Parol, F. J., C. Buriez, G. Brogniez and Y. Fouquart, 1991: Information content of AVHRR Channels 4 and 5 with respect to the effective radius of cirrus cloud particles. *J. Appl. Meteor.*, **30**, 973-984.

Phulpin, T., M. Derrien, and A. Baird, 1983: A two-dimensional histogram procedure to analyze cloud cover from NOAA satellite high resolution imagery. *J. Climate Appl. Meteor.*, **22**, 1332-1345.

Prabhakara, C., R. S. Fraser, G. Dalu, M. C. Wu, and R. J. Curran, 1988: Thin cirrus clouds: seasonal distribution over oceans deduced from Nimbus-4 IRIS. *J. Appl. Meteor.*, **27**, 379-399.

Prabhakara, C., J.-M. Yoo, D. P. Kratz, and G. Dalu, 1993: Boundary layer stratus clouds: inferred from satellite infrared spectral measurements over oceans. *J. Quant. Spectrosc. Radiat. Trans.*, **49**, 599-607.

Rao, C. R. N., L. L. Stowe, and L. L. McClain, 1989: Remote sensing of aerosol over the oceans using AVHRR data: theory, practice, and applications. *Int. J. Remote Sens.*, **10**, 743-749.

Rao, N. X., S. C. Ou, and K. N. Liou, 1995: Removal of the solar component in AVHRR 3.7-μm radiances for the retrieval of cirrus cloud parameters. *J. Appl. Meteor.*, **34**, 482-499.

Raschke, E., P. Bauer, and H. J. Lutz, 1992: Remote sensing of clouds and surface radiation budget over polar regions. *Int J. Remote Sens.*, **13**, 13-22.

Reutter, H. , F. -S. Olesen, and H. Fischer, 1994: Distribution of the brightness temperature of land surfaces determined from AVHRR data. *Int. J. Remote Sens.*, **15**, 95-104.

Revercomb, H. E., H. Buijs, H. B. Howell, D. D. LaPorte, W. L. Smith and L. A. Sromovsky, 1988: Radiometric calibration of IR Fourier transform spectrometers: Solution to a problem with the High-spectral resolution Interferometer Sounder. *Appl. Opt.*, **27**, 3210–3218.

Rossow, W. B., F. Mosher, E. Kinsella, A. Arking, M. Desbois, E. Harrison, P. Minnis, E. Ruprecht, G. Seze, C. Simmer, and E. Smith, 1985: ISCCP cloud algorithm intercomparison. *J. Climate Appl. Meteor.*, **24**, 877-903.

Rossow, W. B., 1989: Measuring cloud properties from space. A review. *J. Climate*, **2**, 201-213.

Rossow, W. B., and A. A. Lacis, 1990: Global and seasonal cloud variations from satellite radiance measurements. Part II: Cloud properties and radiative effects. *J. Clim.*

Rossow, W. B. and L. C. Garder, 1993: Cloud detection using satellite measurements of infrared and visible radiances for ISCCP. *J. Climate*, **6**, 2341-2369.

Rossow, William B. and Leonid. C. Garder, 1993: Validation of ISCCP cloud detections. *J. Climate*, **6**, 2370-2393.

Rossow, William B., Alison W. Walker, and Leonid C. Garder, 1993: Comparison of ISCCP and other cloud amounts. *J. Climate*, **6**, 2394-2418.

Sakellariou, N. K., H. G. Leighton, and Z. Li, 1993: Identification of clear and cloudy pixels at high latitudes from AVHRR radiances. *Int. J. Remote Sens.*, **14**, 2005-2024.

Saunders, R. W., 1986: An automated scheme for the removal of cloud contamination from AVHRR radiances over western Europe. *Int. J. Remote Sens.*, **7**, 867-886.

Saunders, R. W. and K. T. Kriebel, 1988: An improved method for detecting clear sky and cloudy radiances from AVHRR data. *Int. J. Remote Sens.*, **9**, 123-150.

Schmetz, J., C. Geijo, W.P. Menzel, K. Strabala, L. Van De Berg, K. Holmlund, and S. Tjemkes, 1995: Satellite observations of upper tropospheric relative humidity, clouds and wind field divergence. *Beitr. Phys. Atmos.*, Vol. **68**, No. 4, 345-357.

Seze, G. and M. Desbois, 1987: Cloud cover analysis from satellite imagery using spatial and temporal characteristics of the data. *J. Climate Appl. Meteor.*, **26**, 287-303.

Seze, G., and W. B. Rossow, 1991a: Time-cumulated visible and infrared radiance histograms used as descriptors of surface and cloud variations. *Int. J. Remote Sens.*, **12**, 877-920.

Seze, G., and W. B. Rossow, 1991b: Effects of satellite data resolution on measuring the space-time variations of surfaces and clouds. *Int. J. Remote Sens.*, **12**, 921-952.

Simpson, J. J. and J. I. Gobat, 1995: Improved cloud detection in GOES scenes over land. *Remote Sens. Environ.*, **52**, 36-54.

Simpson, J. J., and C. Humphrey, 1990: An automated cloud screening algorithm for daytime advanced very high resolution radiometer imagery. *J. Geophys. Res.*, **95**, 13459-13481.

Smith, W. L. and C. M. R. Platt, 1978: Comparison of satellite-deduced cloud heights with indications from radiosonde and ground-based laser measurements. *J. Appl. Meteor.*, **17**, 1796-1802.

Smith, W. L, 1968: An improved method for calculating tropospheric temperature and moisture profiles from satellite radiometer measurements. *Mon. Wea. Rev.*, **96**, 387.

Spinhirne, J. D., R. Boers and W. D. Hart, 1989: Cloud top liquid water from lidar observations of marine stratocumulus. *J. Appl. Meteor.*, **28**, 81–90.

Stephens, Graeme L., 1980: Radiative properties of cirrus clouds in the infrared region. *J. Atmos. Sci.*, **37**, 435-446.

Stephens, G. L., 1990: On the relationship between water vapor over the oceans and sea surface temperature. *J. Climate*, **3**, 634-645.

Stone, Robert S., Graeme L. Stephens, C.M.R. Platt, and S. Banks, 1990: The remote sensing of thin cirrus cloud using satellites, lidar and radiative transfer theory. *J. Appl. Meteor.*, **29**, No. 5, 353-366.

Stowe, L. L., H. Y. M. Yeh, C. G. Wellemeyer, H. L. Kyle, and the Nimbus-7 Cloud Data Processing Team, 1989: Nimbus-7 global cloud climatology, Part II: First year results. *J. Climate*, **2**, 671-709.

Stowe, L. L., E. P. McClain, R. Carey, P. Pellegrino, G. Gutman, P. Davis, C. Long, and S. Hart, 1991: Global distribution of cloud cover derived from NOAA/AVHRR operational satellite data. *Adv. Space Res.*, **11**, 51-54.

Stowe, L. L., R. M. Carey, and P. Pellegrino, 1992: Monitoring the Mt. Pinatubo aerosol layer with NOAA/11 AVHRR data. *Geophys. Res. Lett.*, **19**, 159-162

Stowe, L. L., S. K. Vemury, and A. V. Rao, 1994: AVHRR clear sky radiation data sets at NOAA/NESDIS. *Adv. Space Res.*, **14**, 113-116.

Stowe, L. L., P. Davis, and E. P. McClain, 1995: Evaluating the CLAVR (Clouds from AVHRR) Phase I cloud cover experimental product. *Adv. in Space Res.*, **16**, 21-24.

Strabala, K. I., S. A. Ackerman, and W. P. Menzel, 1994: Cloud properties inferred from 8-12 μm data. *J. Appl. Meteor.*, **33**, 212-229.

Sun, C., and Wee, W.G., 1983: Neighboring grey level dependence matrix for texture classification. *Comp. Vision, Graphics, Image Proc.*, **23**, 341-352.

Susskind, J., D. Reuter, and M. T. Chahine, 1987: Cloud fields retrieved from analysis of HIRS/MSU sounding data. *J. Geophys. Res.*, **92**, 4035-4050.

Suttles, J. T., R. N. Green, P. Minnis, G. L. Smith, W. F. Staylor, B.A. Wielicki, I. J. Walker, D. F. Young, V. R. Taylor, and L. L. Stowe, 1988: Angular radiation models for Earth-atmosphere system: Volume I - Shortwave radiation. NASA RP 1184, 144 pp.

Takano, Y., K. N. Liou and P. Minnis, 1992: The effects of small ice crystals on cirrus infrared radiative properties. *J. Atmos. Sci.*, **49**, 1487-1493.

Tanré, D., P. Y. Deschanps, C. Devaux, and M. Herman, 1988: Estimation of Saharan aerosol optical thicknesses from blurring effects in Thematic Mapper data. *J. Geophys. Res.*, **93**, 15955-15964.

Tarpley, J. D., 1979: Estimating incident solar radiation at the surface from geostationary satellite data. *J. Appl. Meteor.*, **18**, 1172-1181.

Tjemkes, Stephen A., Leo van de Berg, and Johannes Schmetz, 1996: Simultaneous observations of cold clouds in METEOSAT water vapour and infrared window channel. Submitted to *Contr. to Atmos. Phys.* for publication as a note.

Tovinkere, V. R., M. Penaloza, A. Logar, J. Lee, R. C. Weger, T. A. Berendes, and R. M. Welch, 1993: An intercomparison of artificial intelligence approaches for polar scene identification, *J. Geophys. Res.*, **98**, 5001-5016.

Udelhofen, Petra M. and Dennis L. Hartmann, 1995: Influence of tropical cloud systems on the relative humidity in the upper troposphere. *J. Geophys. Res.*, **100**, 7423-7440.

Vane, G., R. O. Green, T. G. Chrien, H. T. Enmark, E. G. Hansen, and W. M. Porter, 1993: The Airborne Visible/Infrared Imaging Spectrometer (AVIRIS). *Remote Sens. Environ.*, **44**, 127–143.

Vidal, A., 1991: Atmospheric and emissivity correction of land surface temperature measured from satellite using ground measurements or satellite data. *Int. J. Remote Sens.*, **12**, 2449-2460.

Wang, J., and W.B. Rossow, 1995: Determination of cloud vertical structure from upper-air observations. *J. Appl. Meteor.*, **34**, 2243-2258.

Warren, S. G., 1984: Optical constants of ice from the ultraviolet to the microwave. *Appl. Opt.*, **23**, 1206-1225.

Welch, R. M., S. K. Sengupta, A. K. Goroch, P. Rabindra, N. Rangaraj, and M. S. Navar, 1992: Polar cloud and surface classification using AVHRR imagery: An intercomparison of methods, *J. Appl. Meteor.*, **31**, 405-420.

Welch, R. M., K. S. Kuo, S. L. Sengupta, 1990: Cloud and surface textural features in polar regions. *IEEE Trans. Geosci., and Remote Sens.*, **28**, 520-528.

Welch, R. M., M. S. Navar, and S. K. Sengupta, 1989: The effect of spatial resolution upon texture-based cloud field classifications. *J. Geophys. Res.*, **94**, 14767-14781.

Welch, R.M., et al., 1988: Cloud field classification based upon high spatial resolution textural features, Part 1, Gray level cooccurrence matrix approach. *J. Geophys. Res.*, **93**, 12663-12681.

Wielicki, B. A., and J. A. Coakley, 1981: Cloud retrieval using infrared sounder data: Error analysis. *J. Appl. Meteor.*, **20**, 157-169.

Wylie, D. P., and W. P. Menzel, 1989: Two years of cloud cover statistics using VAS. *J. Climate Appl. Meteor.*, **2**, 380-392.

Wylie, D. P., W. P. Menzel, H. M. Woolf, and K. I. Strabala, 1994: Four years of global cirrus cloud statistics using HIRS. *J. Climate*, **7**, 1972-1986.

Yamanouchi, T., K. Suzuki, and S. Kawaguci, 1987: Detection of clouds in Antarctica from infrared multispectral data of AVHRR. *J. Meteor. Soc. Japan*, **65**, 949-962.

Appendix A. Acronyms

ACARS	ARINC (Aeronautical Radio Inc.) Communications, Addressing and Reporting System
AERI	Atmospheric Emitted Radiation Interferometer
AEROCE	Aerosol/Ocean Chemistry Experiment
AERONET	Aerosol Robotic Network
AirMISR	Airborne MISR
AIRS	Atmospheric Infrared Sounder
AMSU	Advanced Microwave Sounding Unit
APOLLO	AVHRR (Advanced Very High Resolution Radiometer) Processing scheme Over cLoud Land and Ocean
ARM	Atmospheric Radiation Measurement Program
ARMCAS	Arctic Radiation Measurements in Column Atmosphere-surface System (Beaufort Sea, Alaska, June 1995)
ASTEX	Atlantic Stratocumulus Transition Experiment (Azores, June 1992)
ASTER	Advanced Spaceborne Thermal Emission and Reflection radiometer
AVHRR	Advanced Very High Resolution Radiometer
AVIRIS	Airborne Visible/Infrared Imaging Spectrometer
CAR	Cloud Absorption Radiometer
CART	Clouds and Radiation Testbed
CEPEX	Central Equatorial Pacific Experiment (Fiji, February-March 1993)
CERES	Clouds and the Earth's Radiant Energy System
CHAPS	Collocated HIRS/2 and AVHRR Processing Scheme
CLAVR	Cloud Advanced Very High Resolution Radiometer
CLS	Cloud Lidar System
COARE	Coupled Ocean-Atmosphere Response Experiment
DAO	Data Assimilation Office (Goddard Space Flight Center)
EOS	Earth Observing System
EOSDIS	EOS Data and Information System

FIRE	First ISCCP Regional Experiment (California, June-July 1987, Beaufort Sea, Alaska, April-June, August 1998)
FOV	Field of View
GAC	Global Area Coverage
GLAS	Geoscience Laser Altimeter System
GLI	Global Imager
GOES	Geostationary Operational Environmental Satellite
HIS	High-spectral resolution Interferometer Sounder
HIRS	High Resolution Infrared Radiation Sounder
HSB	Humidity Sounder from Brazil
ILAS	Improved Limb Atmospheric Spectrometer
ISCCP	International Satellite Cloud Climatology Project
LASE	Lidar Atmospheric Sensing Experiment
LBA	Large Scale Biosphere-Atmosphere Experiment in Amazonia
MAS	MODIS Airborne Simulator
MAST	Monterey Area Ship Tracks Experiment (Monterey and nearby Pacific Ocean, June 1994)
McIDAS	Man-computer Interactive Data Access System
MISR	Multi-angle Imaging Spectro-Radiometer
MOBY	Marine Optical Buoy
MODIS	Moderate Resolution Imaging Spectroradiometer
NAST	NPOESS Aircraft Sounding Testbed
NCAR	National Center for Atmospheric Research
NDSI	Normalized Difference Snow Index
NDVI	Normalized Difference Vegetation Index
NPOESS	National Polar Orbiting Environmental Satellite System
POLDER	Polarization and Directionality of Earth's Reflectances
RAMS	Radiation Measurement System (NASA Ames Research Center and Scripps Institution of Oceanography)

SCAR-A	Sulfate, Clouds and Radiation–Atlantic (Delmarva Peninsula and near-by Atlantic Ocean, July 1993)
SCAR-B	Smoke, Clouds and Radiation–Brazil (Brazil, August-September 1995)
SCAR-C	Smoke, Clouds and Radiation–California (Pacific Northwest, September 1994)
SCF	Science Computing Facility
SeaWiFS	Sea-viewing Wide Field-of-view Sensor
SHEBA	Surface Heat Budget of the Arctic Ocean
SST	Sea Surface Temperature
SUCCESS	Subsonic Aircraft Contrail and Cloud Effects Special Study (April-May 1996)
TARFOX	Tropospheric Aerosol Radiative Forcing Observational Experiment (Delmarva Peninsula and near-by Atlantic Ocean, July 1996)
TIROS	Television and Infrared Observation Satellite
TLCF	Team Leader Computing Facility
TM	Thematic Mapper
TOGA	Tropical Ocean Global Atmosphere
TOMS	Total Ozone Mapping Spectrometer
TOVS	TIROS-N Operational Vertical Sounder
WINCE	Winter Cloud Experiment
WMO	World Meteorological Organization